RSC Advances

PAPER

View Article Online
View Journal | View Issue

Cite this: *RSC Adv.*, 2026, **16**, 27765

Enhancing the hydrophobicity and mechanical integrity of lignocellulosic paper through synergistic integration of terpene-phenolic resin and phosphate waste rock

Oumaima Bendalahcen,[a] Rachid Bouhfid,*[b] Abou El kacem Qaiss,[a] Jones Alami,[a] Mounir EL Achaby *[a] and Fatima-Zahra Semlali *[a]

This study presents a sustainable approach for producing high-performance paper materials by utilizing polysaccharide-rich agricultural residues and inorganic mining by-products. Date palm fibers were chemically and mechanically treated to lower lignin content and enrich cellulose, thereby increasing fiber crystallinity and enhancing interfacial reactivity. These cellulose-enriched fibers served as the foundation for a reinforced paper structure incorporating phosphate waste rock (PWR), assessed here for the first time as a functional additive in papermaking. PWR, rich in calcium and magnesium oxides, interacts with polysaccharide hydroxyl groups, promoting hydrogen bonding and strengthening fiber cohesion. To further modify the surface, a bio-based terpene phenolic resin (TPR) was applied as a coating, introducing additional hydrogen bonds and potential ester linkages with exposed polysaccharide chains. Thermocompression further densified the material and enhanced internal bonding. The resulting paper demonstrated remarkable properties, including a water contact angle of 120° after 60 seconds, and significant gains in rigidity (125%), and tensile strength (74%), along with an increase in ductility (50%). The combined use of phosphate mining by-products, terpene phenolic resin, and thermocompression improves the morphological, thermal, mechanical, and barrier characteristics of cellulose-based materials by leveraging the natural reactivity of polysaccharides and the binding properties of residual lignin.

Received 3rd March 2026
Accepted 12th May 2026

DOI: 10.1039/d6ra01818a

rsc.li/rsc-advances

1. Introduction

The increasing demand for consumer goods and products has led countries around the world to expand their restrictions on plastic, moving beyond just bags to include single-use items such as straws and plastic cups, as these disposable plastic items are considered highly problematic and among the primary contributors to environmental damage.[1–4] The limited use of plastic has intensified research into renewable, biodegradable alternatives.[5,6]

Among sustainable resources, lignocellulosic biomass has emerged as a highly promising and abundantly available resource for developing next-generation bio-based materials.[7] This biomass, primarily composed of cellulose, hemicellulose, and lignin, constitutes the structural backbone of plant cell walls and exhibits considerable potential for conversion into functional products suited for advanced applications, particularly in sustainable paper and packaging industries.[8,9] Each component of lignocellulose contributes distinct structural and functional properties. Cellulose, the most abundant organic polymer on Earth,[10–12] is composed of linear β-1,4-linked D-glucose units.[13] These chains assemble into crystalline microfibrils stabilized by extensive hydrogen bonding, providing exceptional mechanical strength, thermal stability, and chemical resistance.[14] In contrast, hemicellulose is an amorphous, branched polysaccharide that enhances fiber flexibility and water retention.[15] Lignin, the third major component, is a complex, crosslinked aromatic polymer derived from *p*-coumaryl, coniferyl, and sinapyl alcohols. It serves as a natural adhesive, imparting hydrophobicity, UV stability, and thermal resistance to plant structures.[16] Although lignin comprises up to 30% of lignocellulosic biomass, less than 2% is currently valorized in high-end applications, with most being incinerated as waste.[17] Its inherent properties make lignin a valuable candidate for bio-based coatings and structural reinforcements, especially in paper and packaging.[18]

[a]*College of Chemical Sciences and Engineering (CCSE), Department of Materials Science, Energy and Nano-engineering (MSN), Mohammed VI Polytechnic University (UM6P), Lot 660 – Hay Moulay Rachid, 43150, Ben Guerir, Morocco. E-mail: fatimazahra.semlali@um6p.ma; rachid.bouhfid@um6p.ma; mounir.elachaby@um6p.ma*

[b]*International Water Research Institute (IWRI), Mohammed VI Polytechnic University, Lot 660 – Hay Moulay Rachid, 43150, Benguerir, Morocco*

Date palm residues, particularly the fronds and leaflets, represent abundant lignocellulosic waste in arid and semi-arid regions. Their naturally high lignin content and fibrous morphology make them suitable for material applications. When subjected to alkali and mechanical treatments, these fibers undergo partial lignin removal and fiber defibrillation, leading to enhanced interfiber bonding and water resistance. Notably, Wang *et al.*,[19] demonstrated that unbleached bamboo pulp containing 13% residual lignin exhibited greater wet strength and mechanical durability than bleached pulp. Similarly, Semlali *et al.*[18] showed that retaining lignin after alkali treatment preserved aromatic structures that contributed to thermal stability, flame retardancy, and mechanical performance in packaging papers. Mechanical treatments further refine the fibers, increasing their surface area, enhancing accessibility of reactive sites, and maintaining a higher lignin content in the final pulp.[20] Unlike chemical pulping, mechanical pulping produces high-yield pulps, achieving yields as high as 97–98%.[21] This process results in a wide distribution of particle sizes, which improves the optical and surface properties of the paper.[22]

Building on the intrinsic potential of these fibers, one promising pathway lies in transforming them into functional papers and packaging materials, offering a biodegradable alternative to conventional plastics. At this stage, additional treatment steps become essential to refine the physical and surface properties of the resulting bio-based papers. Among these, thermocompression has emerged as a key technique.[23–25] Various studies have examined how factors such as temperature, pressure, and molding time influence the mechanical properties of paper. For instance, Tove Joelsson *et al.*[26] found that when the lignocellulosic pulp is pressed at temperatures above lignin's glass transition temperature (T_g), the lignin within the material acts as a natural wet-strengthening agent. As a result, the wet strength of the pulp can remain stable in water for over 24 hours. This makes the thermocompression technique a distinctive method for producing robust, eco-friendly packaging from renewable and biodegradable lignin-rich raw materials. In other words, the existing lignin in the lignocellulosic pulp exhibits thermoplastic behavior during thermocompression, particularly when the temperature exceeds its glass transition temperature (T_g). This allows lignin to flow and fill voids between fibers, leading to better fiber-to-fiber bonding and creating a denser structure that is less permeable to water, which improves the strength, dimensional stability, and hydrophobicity of papers.[24,27–29]

However, fibers alone are insufficient to achieve the desired chemical and physical properties in paper. Therefore, various mineral additives are used in papermaking to improve the mechanical strength and functionality of the paper. Jung Soo Han *et al.*[30] investigated a flexible calcium carbonate filler that increases tensile strength and enhances paper smoothness due to its deformable nature under pressure. More minerals are being investigated to improve paper properties, such as clay, Talc, and silica ….[31–34] In addition to those conventional mineral additives, mining by-products represent another source of valuable materials that can be used in paper production.[35] These materials are rich in metal oxides and can serve as fillers while also interacting favorably with residual lignin to create composite papers with improved thermal and mechanical integrity.[36,37] For example, phosphate waste rocks (PWR) from Morocco, a country with over 70% of global phosphate reserves,[38,39] are rich in calcium and magnesium oxides.[40] These oxides are known to form hydrogen and electrostatic bonds with phenolic and carboxylic groups in lignin.

However, even with the use of additives, paper still has other limitations. As mentioned, the main component in paper is typically lignocellulosic fibers, constituting 40 to 90% of the paper by weight,[41] which makes it highly hydrophilic and porous, leading to the absorption and transport of water, gases, oils, and fats. A coating process inducing wettability and barrier characteristics is required to produce more effective and performant cellulosic paper packaging materials. Barrier coatings for paper packaging mainly use inexpensive and widely available petroleum-derived or synthetic polymers like polyolefins, waxes, ethylene vinyl alcohol (EVOH), and polyvinylidene chloride (PVDC). These materials provide excellent barriers against water and oxygen, making them well-suited for packaging applications.[42,43] However, they pose significant environmental and economic challenges due to the limited supply of fossil oils, the poor recyclability of coated papers, and their lack of biodegradability. As a result, there has been a shift towards exploring sustainable alternatives, such as water-based coatings, which are more environmentally friendly as they use water instead of volatile organic compounds (VOCs).[44,45] Terpene phenolic resin is gaining traction as a sustainable option for coatings. Derived from renewable resources, it boasts low volatile organic compound (VOC) emissions, making it an environmentally friendly choice compared to other resin types. This thermosetting resin is produced through the copolymerization of a terpene unit and a phenol unit.[46] The synthesis of terpene phenolic resin (TPR) involves two main steps. First, the terpene undergoes a Friedel–Crafts reaction, leading to the formation of a carbocation. This protonated terpene, often isoprene, then reacts with phenol to form the resin, see Fig. 1.[47] TPR is known for its excellent compatibility and solubility in

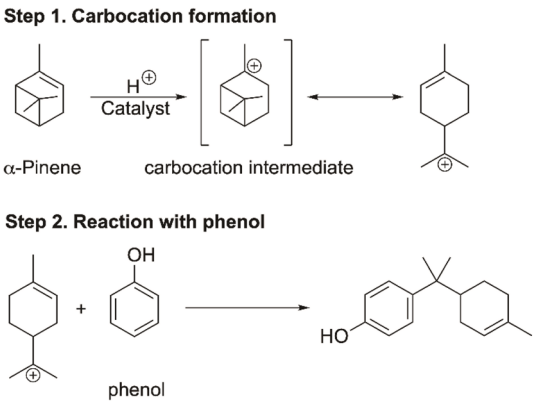

Fig. 1 Synthesis mechanism of terpene phenolic resin from α-pinene and phenol.

both polar and nonpolar solvents.[47] Additionally, it exhibits strong interfacial compatibility with lignocellulosic fibers due to its aromatic structure, and more importantly, it interacts favorably with residual lignin. The phenolic moieties in both lignin and TPR allow for hydrogen bonding and π–π stacking interactions, facilitating uniform coating and enhancing barrier performance.

Despite growing advancements in bio-based material development, there remains a significant gap in understanding the role of residual lignin in composite performance, particularly in its interactions with mineral fillers and bio-based coatings under thermocompressive conditions. The present study investigates the fabrication of biodegradable paper sheets using alkali- and mechanically treated date palm fibers rich in residual lignin. For the first time, phosphate waste rocks (PWR) are introduced as mining byproduct reinforcements, while terpene phenolic resin (TPR) is applied as a sustainable coating. Thermocompression serves as the integration platform, activating lignin's thermoplastic behavior and enabling effective bonding among the paper matrix, fillers, and coating. This research aims to assess how these four factors (lignin, PWR, TPR, and thermocompression) affect the cellulosic paper's morphological structure, thermal properties, hydrophobicity, and mechanical strength.

2. Materials and methods

2.1 Materials

The dried date palm leaves used in this study were obtained from palm trees grown in Morocco. Phosphate waste rocks (PWR), used as mineral particles, were provided in the form of a dry particle from Morocco phosphate beneficiation plant (OCP, Youssoufia). As coating polymer, Dermulsene TR 602, an aqueous, solvent-free resin based on terpene phenolic resin (55 wt%) with a density of 1.02 at 20 °C, a Brookfield viscosity of 800 mPa s at 20 °C, and a pH of 8 at 20 °C was provided by Intercolle, Casablanca, Morocco. Sodium hydroxide (NaOH, >97%) was purchased from Sigma-Aldrich. All the materials were used without any further modification.

2.2 Waste rock preparation

The as-received phosphate waste rock (PWR) had a whiteness index of 60.61 ± 1.96, according to American Standard (ASTM), and a density of 2.8274 g cm^{-3}. The rock was ground using a RETSCH-TM 300 drum mill and then sieved on a (Fritsch Analysette 3 PRO) sieve shaker equipped with a 63 μm sieve.

2.3 Fiber's preparation

The leaves obtained from date palm trees (DPF) were rinsed with tap water and air-dried for 24 hours. The leaves were then grinded using a Fritsch Pulverisette-19 equipped with a 1 mm sieve opening. Subsequently, they were soaked overnight at room temperature in an aqueous NaOH solution (6 wt%) to partially remove lignin, hemicelluloses, and surface impurities from the outer surface of the fiber cell walls.[48,49] Thereafter, the fibers were mechanically processed using a BIOBASE homogenizer model BK-Y50-PLUS at 20 000 rpm for 15 minutes. This process is a fluid mechanical process that uses pressure to achieve high-yield fiber extraction, presenting an energy-efficient method to produce cellulose microfibers.[50,51] Finally, the obtained mechanically treated alkaline date palm fibers (AT/DPF-MT) were washed with tap water through a 63 μm sieve to prevent fiber loss.

2.4 Determination of chemical composition of fibers

The chemical composition of raw date palm fibers (DPF) and mechanically treated alkaline date palm fibers (AT/DPF-MT) was characterized according to standardized TAPPI (Technical Association of the Pulp and Paper Associations) protocols. Samples were conditioned in accordance with TAPPI T257. Ash content was determined by calcinating 2 g of oven-dried sample in a muffle furnace, with the temperature ramped from 100 °C to 525 °C at 2 °C min^{-1} until complete carbonization. Ash percentage was calculated using the formula: ash (%) = $(w_f/w_i) \times 100$, where w_f and w_i are the final and initial dry weights, respectively.

Extractives were quantified using Soxhlet extraction with an ethanol–toluene (1 : 2 v/v) solvent system according to TAPPI T204. Five grams of sample were extracted over 5 h, and the recovered solvent residue was dried at 105 °C to a constant weight. A blank run was conducted for background correction, and extractive content was calculated as: extractives (%) = $[(w_e - w_b)/w_i] \times 100$, where w_e is the extract weight and w_b is the blank residue.

Lignin content was measured following TAPPI T222. Extractive-free samples (2 g) were hydrolyzed with 72% H_2SO_4 at 20 °C for 2 h, diluted to 3%, and boiled for 4 h to isolate acid-insoluble lignin, which was then filtered, dried, and weighed. The lignin content was expressed as: lignin (%) = $(w_l/w_i) \times 100$, with w_l being the lignin mass.

Holocellulose was extracted from extractive-free lignocellulosic fibers through oxidative delignification using sodium chlorite ($NaClO_2$) in the presence of glacial acetic acid at 96 °C, according to the method described by Álvarez *et al.*[52] This procedure allows for the selective removal of lignin while preserving the carbohydrate fraction, comprising both cellulose and hemicellulose, resulting in a holocellulose-rich material suitable for precise structural and compositional analyses.

2.5 Production of cellulosic papers

Paper preparation remains the crucial step for having the desired outcomes. In this study, mixtures of AT/DPF-MT and PWR were prepared at different concentrations (AT/DPF-MT : PWR) (100 : 0; 97.5 : 2.5; 95 : 5; 92.5 : 7.5; 90 : 10; 85 : 15; 80 : 20), respectively. These mixtures were dispersed in water using an Ultra Turrax mixer (IKA, D125 Basic) for 5 min, then spread in a semi-automatic sheet former (Rapid Köthen Sheet Former) from PTE GmbH, Eberstalzell. Typically, each mixture was degassed with a vacuum pump before being filtered, resulting in a uniformly wet cellulosic layer with a diameter of 20 cm, as illustrated in Fig. 2. The wet paper was partially dried in the sheet dryer for 5 min at 95 °C under a pressure of 10 MPa,

Fig. 2 Schematic illustration of the production process for the developed cellulosic paper and coated paper samples.

followed by thermocompression in a semi-automatic heat press (Carver, USA) at 130 °C for 5 min under a pressure of 1 MPa. The resulting papers were labeled UcX, where *X* represents the weight percentage of PWR included (0, 2.5, 5, 7.5, 10, 15, and 20 wt%).

For the preparation of coated papers, after being partially dried in the sheet dryer under the same conditions, each paper type was coated with a pre-prepared aqueous terpene phenolic resin (TPR) solution (2.5 wt%) using a spray coating method before undergoing thermocompression. This compression step at 130 °C for 5 minutes is essential as it ensures both lignin softening and crosslinking of TPR. Confirmed by a study done by Jiang *et al.*,[53] which suggests that the optimal temperature range for hot-pressing lignin without compromising the integrity of the cellulose is between 100 and 130 °C. Thus, terpene phenolic resins experience cross-linking during the curing process, which is a chemical reaction that forms a closely interconnected network of resin molecules and usually takes place at temperatures between 120 °C and 150 °C.[54] Fig. 3 shows that TPRs can also interact with lignin by a variety of other

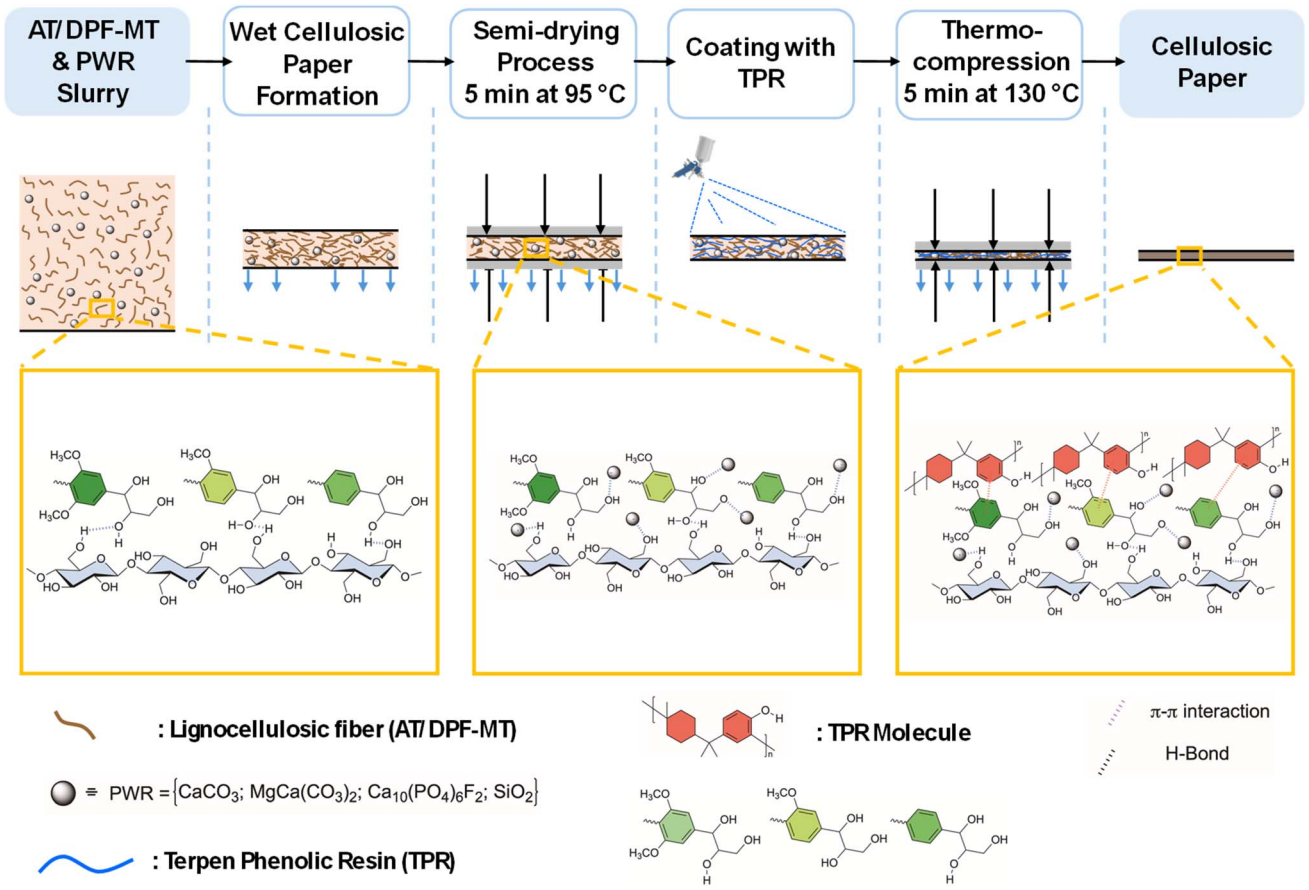

Fig. 3 Schematic representation of the fabrication process and interaction mechanism in the developed cellulosic paper samples.

mechanisms, such as π–π interactions between their aromatic rings[55,56]

The resulting coated papers were denoted as CX, where X indicates the content of PWR. For each formulation, three independent samples were prepared and tested. The reported values represent the mean ± standard deviation.

3. Characterization techniques

3.1 X-ray fluorescence (XRF)

XRF was used to evaluate the chemical composition of PWR particles. The Epsilon 4 X-ray Fluorescence Spectrometer from Malvern Panalytical was used to evaluate about 1 g of the sample.

3.2 X-ray diffraction (XRD)

The identification of mineralogical composition of PWR particle and the crystallinity of elaborated products were performed using a BRUKER D8-Discover powder X-ray diffractometer operating at 40 kV and 100 mA with Ni filter out K_β radiation ($\lambda = 1.5418$ Å). The diffractograms were recorded in reflection geometry using fixed slits, with samples analyzed in powder form on a plastic sample holder. Data were collected over a 2θ range of 5–80°, with a step size of 0.01° and a scan rate of 2° min^{-1}, corresponding to a total acquisition time of approximately 38 min per scan. Background subtraction was performed by baseline correction using Origin software for all XRD patterns prior to crystallinity analysis. Smoothing was applied only to the XRD patterns of raw and alkali-treated date palm fibers to improve signal clarity, while no smoothing was applied to the diffraction patterns of the elaborated cellulosic papers. The crystallinity index (CrI) value was calculated using the Segal peak height method:[57,58] $CrI = (I_{200} - I_{AM}/I_{200}) \times 100$, where the I_{AM} corresponds to the minimum intensity between the $1\bar{1}0/110$ and 200 reflections (around 18.6°), and I_{200} is the maximum intensity of the 200 reflection Background subtraction was performed by baseline correction using Origin software prior to crystallinity analysis.

3.3 Fourier transform infrared spectroscopy (FTIR)

The FT-IR spectra of terpene phenolic resin, as well as the coated and uncoated samples, were obtained using a PerkinElmer Frontier spectrophotometer (FTIR, PerkinElmer Spectrum 2000, Waltham, Massachusetts, United States) operating in the transmittance mode. The experiments were carried out in the range from 4000 to 600 cm^{-1} with a resolution of 4 cm^{-1} and an accumulation of 16 scans.

3.4 Porosity measurements

The porosity of the produced coated and uncoated cellulosic papers was measured using the real and bulk densities of the materials. Thus, the real densities (ρ_r) were determined using the Micro-metrics AccuPyc II 1340 Gas Pycnometer and the bulk densities (ρ_b) were derived from the mass and volume of the samples. An average value was reported based on five samples to provide a representative figure. The rates of porosity (P) were calculated according to prior literature[59,60] using the equation:

$$P(\%) = \frac{\rho_r - \rho_b}{\rho_r} \times 100$$

3.5 Scanning electron microscopy (SEM)

The microstructures of PWR and DPF, along with the surface views of the developed cellulosic papers, were examined using a scanning electron microscope (SEM, ZEISS EVO 10, GmbH, Jena, Germany) at an operating voltage of 10 kV. To avoid electrical charging during imaging, the samples were coated with a layer of gold palladium in an ionization chamber in advance.

3.6 Laser granulometry analysis

To determine the PWR particle size distribution, a Malvern Mastersizer 2000 laser diffraction granulometer equipped with a Hydro 2000 G wet unit was utilized. Distilled water, having a refractive index of 1.33, was used as the dispersant, while PWR's absorption and refractive index were set at 1.53 and 0.1, respectively.

3.7 Thermogravimetric analysis (TGA)

The thermogravimetric analyzer apparatus (Discovery TGA, TA instruments New Castle, United State) was used to assess the thermal stability and degradation (TGA and DTG) of the investigated DPFs, PWR, TPR, and the prepared cellulosic papers. All the analyses were performed under a nitrogen atmosphere (25 mL min^{-1}) at a heating rate of 10 °C min^{-1} from 25 °C to 1000 °C for PWR and from 25 °C to 700 °C for the other products.

3.8 Contact angle measurement

The water contact angle (CA) at an ambient temperature of approximately 22 ± 2 °C and relative humidity of 40 ± 5% was measured using an optical video contact angle system (OCA 40, Dataphysics, Germany) equipped with a CCD camera and SCAT commercial software for image capture. The temporal influence on the CA readings was assessed at intervals of 0, 5, 10, 15, 30, and 60 seconds following the application of a water droplet (*e.g.*, 10 μL) onto the cellulosic papers surface using a micro syringe. The average of five readings was taken as the representative value for each sample.

3.9 Tensile test

According to ISO 527-5, tensile tests were performed using a Universal Machine Texture Analyzer (SHIMADZU, Kyoto, Japan) at a temperature of 22 ± 2 °C and relative humidity of 40 ± 5%. The developed cellulosic papers were cut into rectangular shapes with dimensions of 50 mm in length and 10 mm in width. Thus, the gauge length was fixed at 30 mm, and the speed of the moving clamp was 2 mm min^{-1} using a 1 kN load cell. For each sample, three specimens were tested, and the results are reported as mean ± standard deviation. Statistical

comparisons between samples were performed using Student's *t*-test, with differences considered significant at $p < 0.05$.

3.10 Statistical analysis

All experiments were carried out in triplicate unless otherwise specified. The results are expressed as mean ± standard deviation (SD). Statistical comparisons between samples were performed using Student's *t*-test, and differences were considered statistically significant at $p \leq 0.05$.

4. Results and discussion

4.1 Chemical composition of fibers

The chemical composition of date palm fibers (DPF) before and after alkaline and mechanical treatment (AT/DPF-MT), and the measurements were performed twice and reported in Table 1. The result showed that the raw DPF had extractive (12.86%), holocellulose (52.65%), lignin (29.02%), and ash (4.49%). Following treatment, the AT/DPF-MT showed increased holocellulose content (64.18%) and slightly elevated ash (5.17%), while extractive and lignin were reduced to 5.27% and 24.49%, respectively. These results indicate that alkaline treatment selectively removed non-cellulosic components, particularly hemicellulose and lignin, which are more amorphous and alkali-soluble compared to cellulose. The enrichment in cellulose content and reduction of lignin are highly desirable. Cellulose, with its high crystallinity and mechanical strength, constitutes the principal structural component of natural fibers.[61] Increasing its proportion enhances the stiffness, strength, and thermal stability of the fibers,[62] while the partial removal of lignin exposes more hydroxyl groups on the fiber surface, favoring chemical modification and improving fiber-matrix adhesion in composites.[63]

4.2 Characteristics of PWR particles

In investigating the first-time use of PWR particles in the production of cellulosic materials, a detailed examination of their chemical, crystalline, structural, thermal, and morphological characteristics provides valuable insights into their prospective use in paper and packaging applications. The X-ray fluorescence (XRF) analysis of the phosphate waste rock sample (Table 2) reveals a composition dominated by calcium oxide (CaO) at 89.013%, indicating a substantial presence of calcium phosphate minerals, primarily apatite, which aligns with the material's phosphatic nature.[40,64] The presence of magnesium oxide (MgO) at 5.603% suggests the inclusion of magnesium-rich minerals, possibly magnesite or dolomite. The relatively low concentrations of silicon dioxide (SiO_2) at 1.852%, aluminum oxide (Al_2O_3) at 0.161%, and iron(III) oxide (Fe_2O_3) at 0.171% point to a minor presence of silicate and iron minerals, highlighting the purity of the phosphate material in terms of its primary phosphatic composition. Phosphorus pentoxide (P_2O_5) at 2.833% directly reflects the phosphorus content, essential for understanding the economic value and potential applications of the waste rock.[40,64] X-ray diffraction (XRD) analysis (Fig. 4a) further elucidated the mineral composition of PWR, predominantly featuring Dolomite ($CaMg(CO_3)_2$), Calcite ($CaCO_3$), Quartz (SiO_2), and Fluorapatite ($Ca_5(PO_4)_3F$).[65] The FT-IR analysis of PWR (Fig. 4b) provides detailed insights into its molecular structure by identifying specific absorption bands related to different functional groups or chemical bonds within the material. The absorption band around 1413 cm^{-1} is typically associated with the C–O stretching vibrations of carbonate ions (CO_3^{2-}). This indicates the presence of carbonate minerals such as calcite ($CaCO_3$) or dolomite ($CaMg(CO_3)_2$), which are common in sedimentary phosphate deposits.[66,67] The band around 1053 cm^{-1} is indicative of P–O stretching vibrations in phosphate (PO_4^{3-}) groups, characteristic of apatite minerals (*e.g.*, fluorapatite, hydroxyapatite) that are the primary phosphate-bearing minerals in phosphate rocks. The band at 875 cm^{-1} is attributed to O–P–O bending vibrations, which are also related to the presence of phosphate minerals in the rock.[66,67] The absorption near 730 cm^{-1} could be associated with out-of-plane bending vibrations of carbonate ions (CO_3^{2-}), further supporting the presence of carbonate minerals in the phosphate waste rock. It could also be related to specific symmetrical stretching or bending modes of silicate minerals (Si–O–Si) if silicates are present in minor amounts.[66,67]

This correlation between XRF, XRD, and FT-IR analysis aligns with prior studies, affirming the non-hazardous nature of PWR and their similarity to natural aggregates.[68,69] Considering their organic and geotechnical attributes, PWR can be classified alongside conventional natural aggregates.[68,69] Using these materials could impact natural resource conservation by reducing the reliance on extracted materials and promoting the recycling of PWR, thereby facilitating their application as mineral additives in paper and packaging solutions.

The thermal analysis of the PWR in Fig. 4c reveals critical insights into its thermal stability and composition. The TGA curve indicates an initial weight loss up to 100 °C due to the evaporation of physically adsorbed water. The major weight loss

Table 2 Chemical composition of waste rock particles

Major oxides (wt.%)					
MgO	Al_2O_3	SiO_2	P_2O_5	CaO	Fe_2O_3
5.603	0.161	1.852	2.833	89.013	0.171

Table 1 Chemical properties of Raw DPF and AT/DPF-MT

	Extractive (%)	Holocellulose (%)	Lignin (%)	Ashes (%)
Raw DP	12.86 ± 0.1	52.65 ± 0.6	29.02 ± 0.4	4.49 ± <0.1
AT/DPF-MT	5.27 ± <0.1	64.18 ± 0.3	24.49 ± 0.5	5.17 ± <0.1

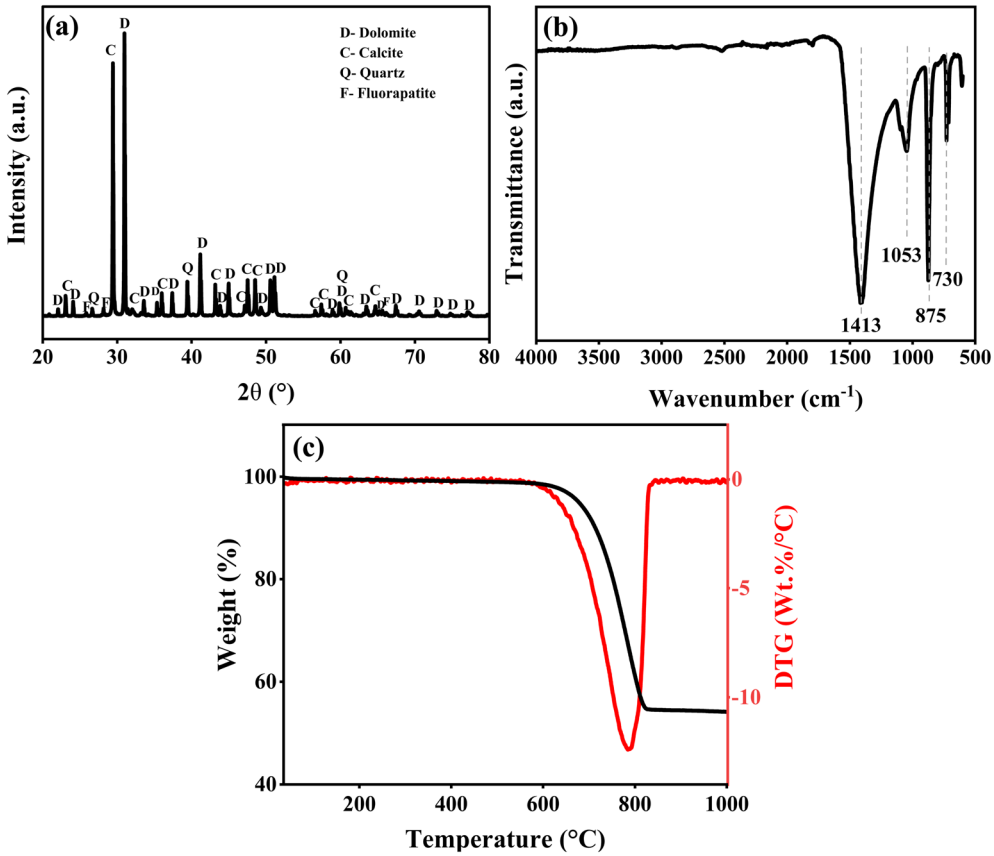

Fig. 4 Crystalline, structural, and thermal characterization of phosphate waste rock (PWR) particles. (a) XRD pattern showing the main crystalline phases. (b) FTIR spectrum indicating characteristic functional groups of carbonate, phosphate, and silicate species. (c) TGA-DTG curves illustrating thermal stability and decomposition behavior.

between 700 °C and 800 °C, indicated by a pronounced peak in the DTG curve around 785 °C, corresponds to the decomposition of carbonate minerals, such as dolomite ($CaMg(CO_3)_2$) and calcite ($CaCO_3$), releasing CO_2.[70] This weight reduction aligns with the carbonate mineral content identified in XRD and FT-IR analyses. Beyond 800 °C, the weight stabilizes, suggesting the presence of thermally stable phosphate minerals like fluorapatite.[70]

SEM analysis and laser granulometry were conducted to examine the morphology and size distribution of PWR particles, as depicted in Fig. 5. The SEM images showed that the particles were mainly composed of large, irregular particles alongside smaller, flat ones. The size distribution showcases a median size (D_{50}) of 11.554 μm, with 90% of particles (D_{90}) smaller than 34.582 μm, confirming the sieving through a 63 μm mesh. Finer particles are known to enhance the smoothness and uniformity of the paper's surface, essential for high-quality printing and writing. Furthermore, the increased surface area promotes fiber bonding, which improves paper strength and durability. This comprehensive particle size analysis emphasizes the potential of PWR as a beneficial filler in the papermaking process, where its finer particles can be used to improve the mechanical and visual quality of paper products.

4.3 Properties of the produced cellulosic papers

4.3.1 Crystalline and chemical structural analysis. Crystallinity plays a crucial role in determining the intrinsic properties of fibers, which in turn can have an impact on the properties of the final material. Therefore, it is important to understand the changes in the crystalline structure and crystallinity index of fibers after different treatments in order to optimize the properties of cellulose-based paper products.[71,72] To this end, X-ray diffraction (XRD) analyses were initially performed on both raw and alkali-treated fibers after the mechanical treatment. Fig. 6a reveals that both types of samples maintain the characteristic cellulose Iβ crystalline structure. The broad diffraction peak observed in the 14–17° region corresponds to the overlapping contributions of the $(1\bar{1}0)$ and (110) planes, while the main peak at approximately 22.5° is assigned to the (200) plane, and the peak at around 34.5° corresponds to the (004) reflection.[73,74] The crystallinity index (CrI) was calculated using the Segal method for these fiber samples, as no mineral interference is present. The alkali treatment was found to increase the cellulose crystallinity from 62.32% to 67.82%, affirming the partial removal of non-cellulosic substances like lignin and hemicellulose, thereby facilitating a more organized arrangement of cellulose chains.[72] This observation is consistent with

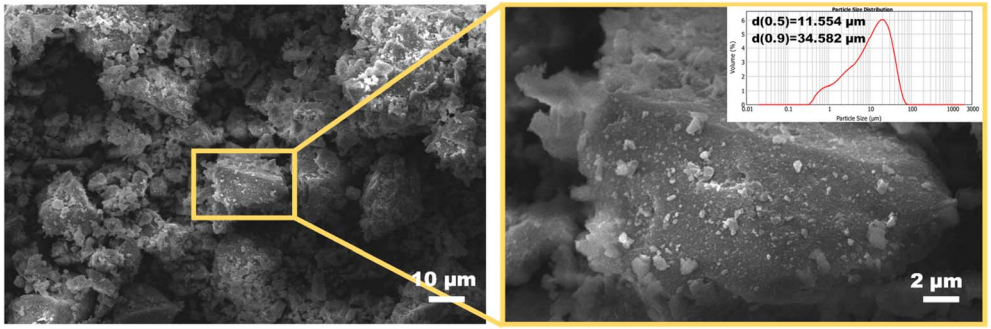

Fig. 5 SEM images at different magnifications showing irregular particle shape, rough surface texture, and agglomeration; inset presents particle size distribution with median diameter (D50).

the chemical composition results obtained according to TAPPI standards (Table 1).

For uncoated and coated cellulosic papers (Fig. 6b), the addition of Phosphate waste rock to cellulosic papers results in the emergence of two crystalline peaks at diffraction angles of 29° and 31°, which correspond to calcite and dolomite, respectively.[65] In addition, PWR exhibits diffraction contributions in the 20–23° region, which overlap with the cellulose (200) peak. As a result, the Segal method cannot be reliably applied to these composite systems. Therefore, a qualitative analysis of the XRD patterns was performed instead. As shown in Fig. 6b, a progressive decrease in the relative intensity of the cellulose (200) peak is observed with increasing PWR content, indicating a disruption of the hydrogen bonding network that is essential for the formation of crystalline regions within the cellulose structure.[75] Furthermore, the incorporation of mineral fillers introduces a non-cellulosic phase, which dilutes the relative fraction of cellulose in the composite, leading to a reduction in the crystal content relative to the total paper mass.[76]

A similar trend is observed following the application of the terpene phenolic resin (TPR) coating. The introduction of the polymeric phase leads to a decrease in the intensity of the cellulose peaks, which can be attributed to both physical and chemical effects. Interactions between TPR and the lignocellulosic matrix, including hydrogen bonding and π–π interactions with lignin,[77,78] may partially disrupt the hydrogen bonding network within cellulose that is essential for crystalline ordering. In addition, the formation of a crosslinked TPR network during curing restricts the mobility and rearrangement of cellulose chains during thermocompression, thereby hindering the development of ordered crystalline regions.

To assess the impact of these reactions on the functional groups and to detail the chemical structure of the resultant lignocellulosic papers, FT-IR analysis was first carried out on the lignocellulosic fibers and the terpene phenolic resin applied. From Fig. 7, initial examinations of raw DPF reveal the existence of the cellulose, hemicellulose, and lignin characteristics peaks. Indeed, the broad peaks located at 3350–3282 cm^{-1} and 2930–2855 cm^{-1} were attributed to O–H stretching and C–H bonds present in the –CH and $–CH_2$ groups of cellulose and hemicellulose, respectively.[79] The band at 1728 cm^{-1} corresponds to the presence of carbonyl groups (C=O), specifically associated with the acetyl groups present in hemicelluloses, while the peak observed at 1604 cm^{-1} was attributed to the bending mode of the absorbed water.[80,81] The peak depicted at 1516 cm^{-1} resulted from lignin's aromatic hydrocarbons' C–C stretching.[82] Additionally, the three peaks at 1425, 1361 and 1317 cm^{-1} are assigned to the symmetric bending of the CH_2 groups in cellulose, the symmetric stretching of the C–O bonds

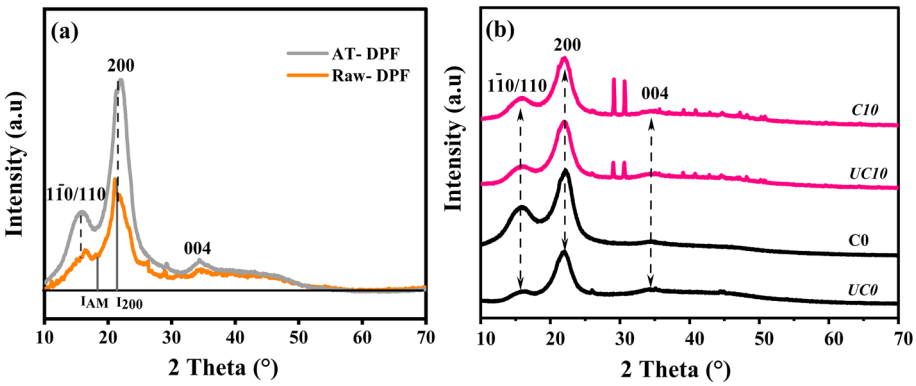

Fig. 6 (a) XRD patterns of raw DPF and alkali-treated DPF (AT-DPF), highlighting the amorphous (I_{am}) and crystalline (I_{200}) peaks used to assess changes in crystallinity after treatment. (b) XRD patterns of the produced paper samples illustrating their structural characteristics.

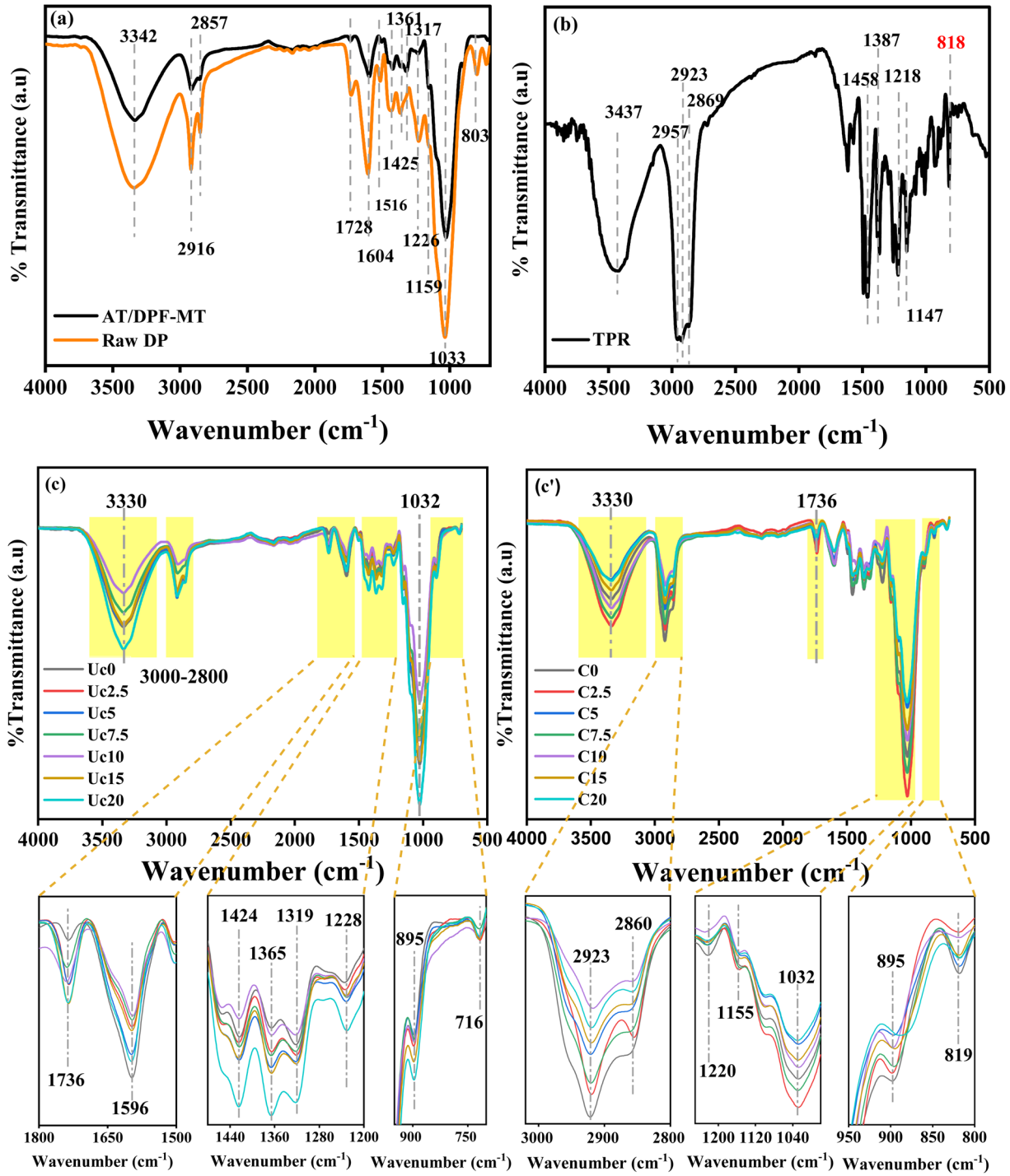

Fig. 7 FTIR spectra of fibers, resin, and paper samples. (a) Spectra of raw and treated fibers. (b) Spectrum of terpene phenolic resin (TPR) highlighting aromatic and hydroxyl-related bands. (c) Spectra of uncoated papers and (c′) coated papers, illustrating the evolution of functional groups and interactions after PWR and TPR incorporation; highlighted regions indicate major absorption bands and their variations among samples.

in the aromatic ring of polysaccharides, and the symmetric deformation of C–H bonds, respectively.[80,83] The (–COO) groups of hemicellulose and the C–O–C asymmetric stretching of cellulose were linked to the peaks at 1226 cm^{-1} and 1159 cm^{-1}, respectively. The final two bands, which were found at 1033 cm^{-1} and 803 cm^{-1}, were associated with the β-(1–4) glucosidic ether linkages (C–O–C), which were connected to the anhydro-glucopyranose ring skeleton's vibration modes, and the β-glycosidic connections between the cellulose's anhydro-glucose rings.[82,84] Furthermore, an analysis of the FTIR spectra of AT/DPF-MT and raw DPF showed a notable drop in the intensity of the hydroxyl (OH) group after the alkali and

mechanical treatments, which was mainly ascribed to the hydroxyl and carboxyl groups forming hydrogen bonds on the fiber's surface.[85,86] This comparison also revealed decreases in peak intensities at wavelengths of 1728, 1604, 1516, and 1226 cm^{-1}. This diminishment supports the expected effects of alkali and mechanical treatments, which notably involve the partial elimination of non-cellulosic substances such as hemicellulose and lignin, ultimately leading to enhanced crystallinity.[60] Finally, after alkaline and mechanical treatment, a new peak at 895 cm^{-1} appeared, which was associated with out-of-plane deformation of the C–H β-glycosidic bond in cellulose.[87] This suggests an increase in the proportion of crystalline cellulose, or structural changes associated with the partial removal of lignin and hemicellulose and the appearance of more cellulose exposed at the surface, as confirmed by XRD.[87]

Noticeable changes in the FT-IR spectra of the resulting materials were observed upon the addition of PWR to the cellulosic papers at varying concentrations (2.5 wt% to 20 wt%), indicating specific interactions and structural modifications (Fig. 7b). Increased hydrogen bonding between the hydroxyl groups of cellulose and hemicellulose and the mineral components of PWR is suggested by the peak intensity rise about 3330 cm^{-1}.[88,89] Because of increased molecular packing brought on by the thermocompression process, peak shifting to lower wavenumbers is probably further encouraged by hydrogen bonding.[90] The decrease in intensity in the 3000–2800 cm^{-1} region may be due to the partial removal of hemicellulose and lignin during the alkali treatment, and the subsequent embedding of these groups within the more rigid structure formed by the interaction with PWR components. This indicates a reduction in the presence or accessibility of methyl and methylene groups.[88,89]

The carbonyl groups in hemicelluloses may be reacting with PWR components to produce new carbonyl-containing compounds throughout the thermocompression process, as suggested by a shift and rise in the peak intensity of 1736 cm^{-1}.[90,91]. The structural integration of PWR inside the lignocellulose matrix is probably improved by this interaction, which may influence the mechanical qualities of the paper. A shift and drop in the peak intensity of 1596 cm^{-1} suggests a decrease in the amount of lignin or a modification of its structure. This could be attributed to the breakdown of lignin during alkali treatment and its interaction with PWR.[90,91] The presence of carbonate minerals such as dolomite or calcite from PWR is indicated by the increase in the peak intensity of 1424 cm^{-1}, which suggests a higher concentration of carbonate ions in the papers.[92] Increases in the 1365 cm^{-1} and 1319 cm^{-1} intensities point to structural alterations in the cellulose and lignin as a result of the interaction with PWR; these alterations could be the result of enhanced crystallinity or altered cellulose chain packing brought on by the presence of mineral particles.[91,92]

A rise in the intensity of 1228 cm^{-1} indicates improved chemical interactions between the PWR components and the cellulose and hemicellulose ether and ester groups.[90] The observed rise in the 1032 cm^{-1} intensity or shifts indicates a possible interaction between the phosphate groups from PWR and greater exposure of the crystalline sections of cellulose.[90] Because more prominent crystalline areas of cellulose are exposed and react with phosphate minerals, the 895 cm^{-1} peak is sharper and more intense.[92] Interactions with silicate or carbonate minerals from PWR are responsible for the formation of a new peak at 716 cm^{-1}, as this band can reflect out-of-plane bending vibrations of carbonate or silicate structures.[92]

All things considered, the addition of PWR demonstrates the chemical and physical interactions that occur between the PWR components and the AT/DPF-MT, as illustrated in Fig. 5. The breakage of native cellulose bonds and the integration of PWR minerals are shown by changes in the intensity and appearance of particular absorption bands, which are indicative of these interactions. The cellulose chains' chemical bonding and alignment inside the paper matrix are further influenced by the thermocompression process, which can improve or change these interactions.

Understanding the impact of terpene phenolic resins as a coating polymer on our cellulosic papers, and analyzing its molecular structure *via* FT-IR spectroscopy, is essential for comprehending their interaction with lignocellulosic fibers in the context of enhancing paper products (Fig. 7c). Specifically, the stretching vibration of the hydroxyl group (C–OH) in the aromatic ring is represented by the peak seen at 3437 cm^{-1}.[93] The stretching vibration of the methyl and methylene groups is responsible for the peaks noticed at 2957 cm^{-1}, 2923 cm^{-1}, and 2869 cm^{-1}.[94,95] Furthermore, the C–H bond's bending vibrations are represented by the absorption peaks at 1458 cm^{-1} and 1387 cm^{-1} [95]. At 1218 and 1147 cm^{-1}, stretching vibrations of the ether carbon–oxygen bond were detected.[96] The range of absorption peaks between 1000–650 cm^{-1}, especially at 819 cm^{-1}, corresponds to planar arrangements of the C–H vibrations, which provide more information about the molecular structure of the resin.[97–99]

As a result, TPR increases hydrogen bonding by introducing more hydroxyl groups from the resin (Fig. 7c′). This could lead to the current O–H stretching peak, which is located at 3330 cm^{-1}, being wider.[100] The intensity of peaks in the regions 2957 cm^{-1}, 2923 cm^{-1}, 2860 cm^{-1}, and 3000–2800 cm^{-1} increases due to the C–H stretching vibrations of TPR's methyl and methylene groups, suggesting the integration of TPR's aliphatic chains with the cellulose matrix.[100] When hemicellulose carbonyl groups interact with hydroxyl groups from TPR, the peak at 1736 cm^{-1} may move or intensify. This represents the emergence of novel chemicals having carbonyl or ester groups.[101] The C–O–C stretching area and variations in peak intensity around 1220 cm^{-1} and 1155 cm^{-1} are attributed to the ether bonds in TPR. This implies that the cellulose fibers and resin have formed ether bonds.[101] A stronger bonding environment for the cellulose chains may be indicated by an increase in the peak intensity at 1032 cm^{-1} due to the interaction of TPR with the glycosidic linkages of cellulose.[101] The intensity of peaks around 895 cm^{-1} and the appearance of a peak at 819 cm^{-1}, indicating the contribution of the resin's aromatic structure to the total matrix, will rise in the presence of aromatic C–H bending vibrations from TPR.[100]

Overall, TPR enhances chemical bonding within the lignocellulose matrix, potentially altering crystalline structures and improving specific properties of the paper, as previously anticipated (Fig. 3). The thermocompression process further enhances these interactions, strengthening the resin's interactions with cellulosic paper and enhancing its overall performance characteristics.

4.3.2 Morphological observations. For examining fiber surface morphology, scanning electron microscopy (SEM) is a crucial method that provides in-depth understanding of microstructural alterations brought about by different treatments. Raw, alkali-treated, and mechanically treated date palm fibers are all shown in Fig. 8's SEM pictures, highlighting the effects of each process on the fibers' morphology. Fig. 8a clearly shows the compact surface of untreated date palm fibers with a diameter of 165 753 ± 0.861 μm, where fibrils are densely packed. It also prominently highlights waxes, oils, and other impurities, typical of the plant's Saharan origin, which act as natural protective coatings on the fiber.[102] Upon alkali treatment (Fig. 8b), the cylindrical shape of the DPF remains largely unchanged, but the treatment effectively removes many surface substances because of their solubility in the NaOH aqueous solution, yielding a cleaner and smoother fiber surface.[103–106] This process notably lowers the fiber diameter to $D = 90\,269 \pm 12\,835$ μm and initiates fibrillation, which exposes more of the fiber's internal structure and enhances its potential for further processing. The mechanical treatment (Fig. 8c) appears to successfully defibrillate fibers. The application of high shear during defibrillation effectively breaks down fibers, reducing their average diameter to 8499 ± 2013 μm. In addition to splitting the fibers longitudinally, this mechanical action also produces a rougher surface. This is helpful in applications where more surface area is needed for better bonding or adhesion in composite materials. These successive treatments

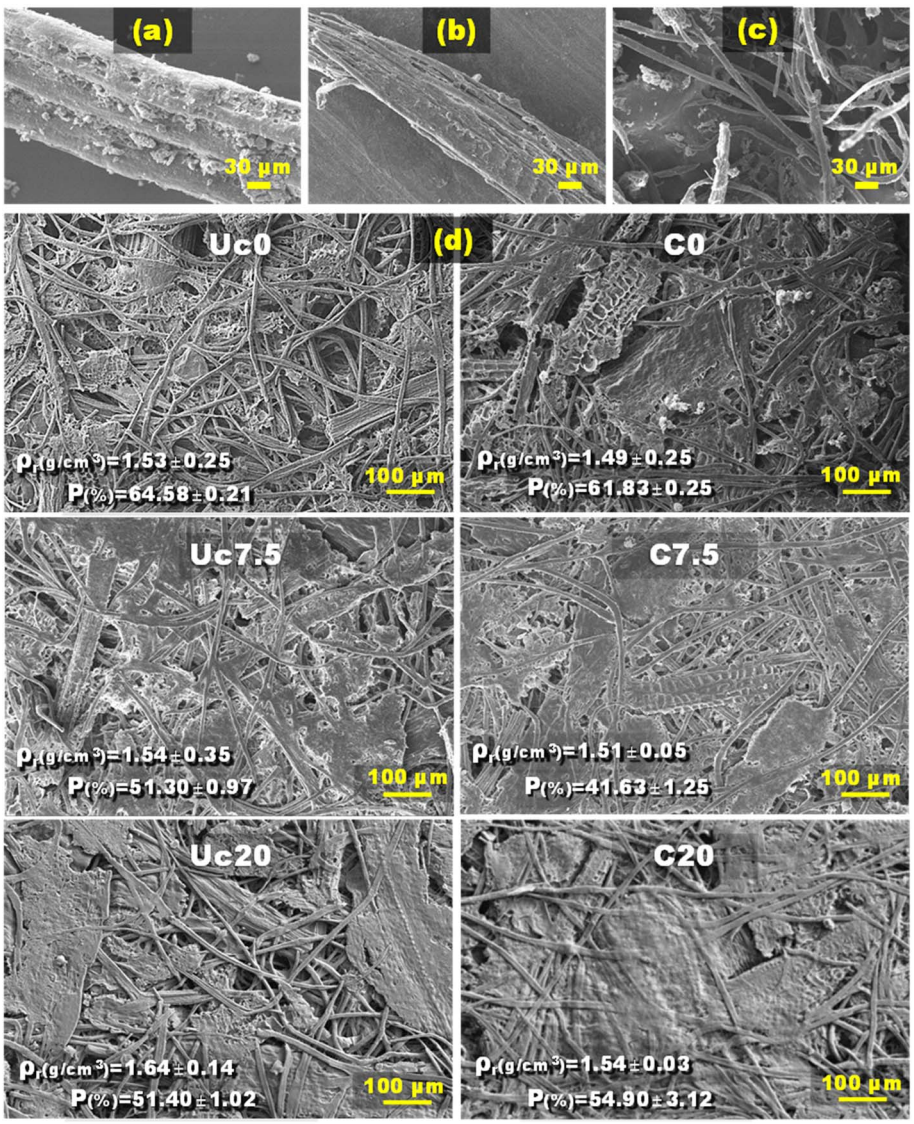

Fig. 8 SEM images of raw fibers (a), alkali-treated fibers (b), the alkali-treated fibers after the mechanical treatment (c), and the uncoated and coated cellulosic papers surface at 0, 7.5 and 20 wt% of PWR content (d), illustrating changes in fiber network structure and porosity, with reel density (ρ_r) and porosity (P) values are indicated.

modify the fibers' structural characteristics in a fundamental way, which is important for improving their performance in later uses, including thermocompression procedures.

The top-view SEM observations of the elaborated papers (Fig. 8d), when correlated with the XRD and FTIR analyses, provide a detailed understanding of the surface morphology and structural properties of the papers. The uncoated and unfilled papers (Uc0) show a surface morphology that is defined by a combination of areas where fibers are exposed and areas where they stick together to form a surface that is relatively continuous. This surface morphology is mainly attributed to the residual lignin on the fiber surface following the alkali and mechanical treatments. Moreover, fiber adhesion is further improved by the thermocompression process at 130 °C. Indeed, the heat supplied during this procedure softens the residual lignin, enabling it to function as a plasticizer, encouraging tighter stacking of cellulose chains and generating a robust physical cross-linked network through intermolecular hydrogen bonding interactions, as confirmed by FT-IR study.[18,107,108] The enhanced crystallinity and the organized structure are also responsible for the smooth surface observed in the SEM images, where some fibers are embedded forming a dense and cohesive layer.[60] The high porosity of approximately 65%, which indicates substantial void spaces between fibers despite adhesion, is indicative of this structural arrangement.

The surface seems more continuous and smoother with less exposed fibers in the SEM pictures of papers containing 7.5 wt% PWR (Uc7.5), suggesting improved fiber adhesion. This enhanced surface morphology, as confirmed by FTIR measurement, is the result of chemical interactions between the PWR's mineral components and cellulose fibers.[90] The successful incorporation of mineral particles into the cellulose matrix filled the gaps between fibers, resulting in a more homogeneous and continuous surface and a reduction in porosity from 65% to 51%, reflecting the reduction in voids.[65] The porosity is slightly increased when PWR is increased to 20 wt% (Uc20) because the dense packing of cellulose fibers is disrupted by the excessive amount of mineral fillers. The mineral particles can produce microvoids and defects in the matrix at high concentration, which serve as pathways for air and moisture and raise the porosity overall.[90] This is seen in the SEM image, when gaps and minor imperfections start to appear on the surface even though it is still mostly smooth.

TPR-coated papers appear to have good fiber adhesion because their surface is smoother, more continuous, and has fewer exposed fibers than uncoated ones. As shown by the FT-IR study, this is first related to the applied resin, which coats the paper's surface in a consistent and cohesive layer. It is also related to their chemical interactions and the successful integration of the resin with the cellulose fibers.[109–111] During the thermocompression curing process, TPR undergoes cross-linking which forms a highly connected network that enhances fiber binding and lowers the porosity of the material.[54]

Nonetheless, the best results in terms of fiber adherence and surface smoothness are obtained when coated cellulosic papers are filled with PWR (C7.5). By combining the beneficial aspects of both materials, PWR and TPR improve the physical characteristics of the paper. PWR's mineral filler functions maintain structural integrity, thus promoting a continuous surface. Concurrently, the TPR coating strengthens the lignocellulose matrix's chemical bonds, resulting in a very cohesive layer. This synergistic combination yields the lowest porosity of 41%, indicating a dense and compact structure ideal for a range of high-performance and sustainable applications. Nevertheless, TPR-coated sheets exhibit an increase of 55% porosity when the PWR concentration is raised to 20 wt%. More fibers are exposed at the surface, further confirming that the excessive amount of mineral fillers is causing micro-voids and irregularities within the matrix. When compared to uncoated and unfilled papers, the coating still improves fiber adherence and overall surface smoothness despite the higher porosity.

4.3.3 Thermal stability. Cellulosic papers' applicability for a variety of uses, including packaging, is greatly influenced by their thermal stability.[60] The effects of alkali and mechanical treatment on fiber thermal stability were examined using TGA, which was then used to examine the effects of PWR addition and TPR coating. These findings were combined with the advantages that the thermocompression process provides for the thermal and degradation properties of the paper samples that are produced. Fig. 9a shows the degradation behavior and thermal stability of both DPF and AT/DPF-MT. At close to 100 °C, both types of lignocellulosic fibers show an initial weight loss of roughly 5%, which is related to the physical moisture on the surface evaporating. The raw DPFs degrade in two stages, with an onset degradation temperature (T_{onset}) of 218 °C and maximum temperatures (T_{max1}) and (T_{max2}) of 271 °C and 342 °C, respectively. Hemicellulose and lignin are responsible for the first degrading stage, whereas cellulose is responsible for the second.[112] After subjecting the fibers to alkali and mechanical treatments, the Tonset rises to 268 °C, the T_{max1} is hardly detectable at 287 °C, while the T_{max2} rises noticeably to 352 °C. Since hemicellulose and lignin breakdown normally occurs at lower temperatures, this shift suggests that the majority of these components have been efficiently eliminated by the alkali treatment, because their degradation at relatively low temperature was roughly detected in AT/DPF-MT sample. The presence of ash and lignin in the untreated fibers is the reason for the increased residue proportion in raw DPF at elevated temperatures when compared to AT/DPF-MT.[112]

Lignocellulosic papers' structural qualities and thermal stability are further improved by the addition of PWR in conjunction with the thermocompression process (Fig. 9c and c′). The major degradation peak temperature (T_{max}) climbs from 352 °C to 355 °C, and the T_{onset} grows from 298 °C to 309 °C as the PWR content increases from 0 to 20 wt%. The high concentration of thermally stable minerals in PWR, such as calcium oxide (CaO) and magnesium oxide (MgO), is the main cause of this augmentation, as supported by the particles XRF.[40,64] This increased thermal stability is mostly due to the major presence of magnesium-rich minerals like dolomite and magnesite, as well as calcium phosphate minerals like apatite, which are noted for their high thermal stability.[40,64] Another important element is the rise in char content that occurs with

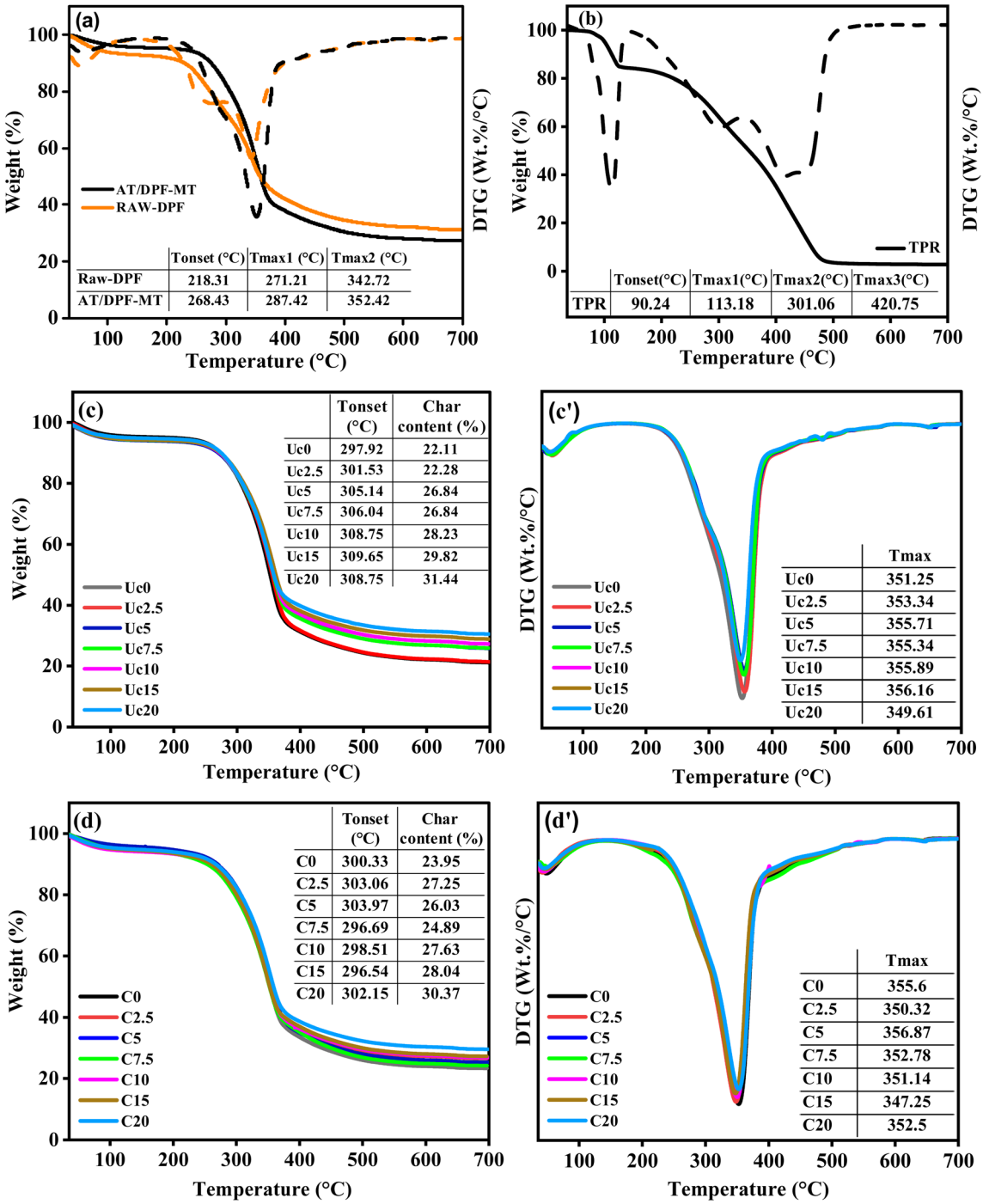

Fig. 9 (a) Thermal curves of raw and alkali-treated fibers. (b) Terpene phenolic resin (TPR). (c) Uncoated papers and (c′) their derivative curves. (d) Coated papers and (d′) their derivative curves at different PWR contents. Key thermal parameters, including onset temperature, maximum degradation temperature, and char residue, are summarized in the inset tables.

the addition of PWR. Carbonaceous residues are stabilized by the high CaO content, while stable char production is encouraged by the MgO. Furthermore, the breakdown of carbonate minerals like calcite and dolomite produces stable oxides that promote the production of char, which is in good correlation with the XRD and TGA results of PWR.[70] The combined effect of these elements improves the overall performance and thermal stability of the lignocellulosic sheets.

In order to fully understand the impact that TPR coating can have on the overall characteristics of the paper, an investigation into its thermal stability was required. Thus, three-step decomposition stages were shown by the TGA curves (Fig. 9b): an initial rapid weight loss around 113 °C brought on by the release of extraneous water, free aldehyde, and phenol.[113] A more gradual mass reduction at 301 °C was explained by the condensation reaction that produced the crosslinked network

structure. The last stage above 420 °C involves the precipitation of organic compounds from the reaction of residual functional groups.[113] The aforementioned phases demonstrate the elimination of volatile substances, the establishment of a robust crosslinked structure, and the breakdown of high molecular weight polymers. The TGA data also show a small amount of residual char at the end of the thermal degradation process, indicating that some organic molecules in TPR disintegrate but leave behind some residue. This residual char suggests that TPR has an impact on char formation to some extent, which may offer the underlying materials enhanced thermal protection.[113,114]

Hence, coating the produced lignocellulosic papers with TPR somehow enhances the overall product heat stability (Fig. 9d and d′). On the paper's surface, the TPR coating creates a uniform and cohesive layer that is cross-linked to form a highly connected network during the thermocompression curing process, as supported by SEM results. By improving fiber binding and decreasing porosity, this network strengthens the material's resilience to heat deterioration.[109–111] The char layer created by the TPR coating serves as a barrier, preventing heat and more thermal degradation from reaching the cellulose fibers underneath.[113,114]

To sum up, the integration of PWR addition, thermocompression, and TPR coating yields better thermal properties in lignocellulosic papers, making them more appropriate for high-performance and environmentally friendly uses. These improvements highlight the possibility of enhancing the performance and longevity of cellulosic composites by using mining by-products and advanced coating methods.

4.3.4 Contact angle analysis. One well-known drawback of cellulosic materials is their susceptibility to water and moisture. Surface roughness, surface heterogeneity, or the absorption of the droplet liquid into the material's bulk can all have an impact on contact angle hysteresis.[115] One important measure of a material's hydrophilicity or hydrophobicity is its water contact angle (CA), with smaller angles denoting greater hydrophilicity and higher angles denoting greater hydrophobicity.[115]

In order to completely understand the wetting behavior of the produced cellulosic papers, it is imperative to take into account both static and dynamic contact angle data. While static tests give an instantaneous picture of a material's hydrophilicity or hydrophobicity, analyzing the dynamic behavior over time reveals more about the material's real–world interactions with water.[116] This is especially important for applications where performance can be greatly impacted by time-dependent wetting behavior, such as packaging.[116] For a more thorough understanding of the material's performance and durability in moisture-sensitive situations, both static and dynamic contact angle analysis is necessary. Hence, Fig. 10a shows the initial contact angle determined within 0–1 second of applying water droplets, while Fig. 10b presents the contact angle values at specific time intervals (0, 5, 10, 15, 30, and 60 seconds).

The results show that all uncoated papers have an initial contact angle exceeding 109°, peaking at 119° for the Uc0. This high initial contact angle can primarily be attributed to alkali and mechanical treatments of the fibers surface, which enhance surface roughness and remove amorphous components. This exposure of more crystalline cellulose contributes to the paper's ability to initially repel water, thanks to its structured surface.[18] Additionally, the residual lignin acts as a hydrophobic barrier. Since lignin is inherently hydrophobic, its presence on fiber surfaces contributes to the high initial contact angles observed. Lastly, the process of thermocompression, which softens the lignin, allows it to flow and coat the fibers more uniformly. This results in a smoother, denser, and more compact structure, enhancing the paper's resistance to water absorption.[18]

Higher contact angles are maintained when PWR is added in amounts ranging from 0 to 20 wt%. This is because the chemical interactions between the lignin, cellulose, and PWR's mineral components lower the whole material's surface energy, creating a strong and stable hydrophobic surface.[90] The mineral particles in PWR, on the other hand, may introduce surface heterogeneity, disrupting the uniform hydrophobic layer formed by lignin and cellulose, and increasing the surface energy at localized spots. This is the main reason for the slight

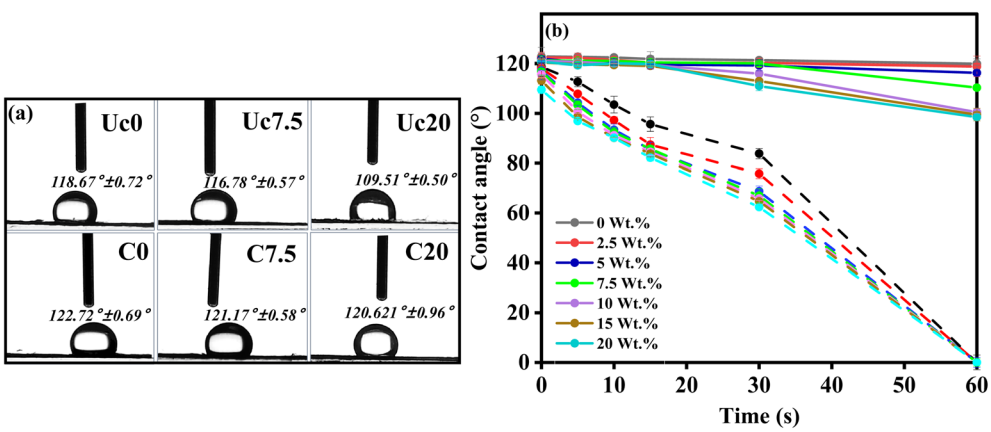

Fig. 10 (a) Static water contact angle measurements for the produced cellulosic papers. (b) Dynamic water contact angle measurements for the produced cellulosic papers. (- - - uncoated; ____ coated).

decrease in the initial contact angle from 119° to 109°.[53] As opposed to organic materials like lignin, mineral fillers usually have higher surface energy. The surface is somewhat more hydrophilic than the unfilled samples because of the improved interactions with water molecules induced by the higher surface energy.[117] Furthermore, PWR addition may cause surface micro-roughness. Through the Cassie–Baxter effect, a certain amount of roughness can promote hydrophobicity; however, too much roughness can cause the Wenzel state, in which water permeates the roughness grooves and increases wettability.[118] The fact that the surface treatments only produce temporary hydrophobicity is indicated by the shift from a high initial contact angle to total absorption over time. High contact angles are the initial outcome of the hydrophobic surface that lignocellulose and PWR combine to generate, which efficiently repels water.[118] Yet with time, water penetrates the material due to capillary action and the inherent porosity of the cellulose fibers, decreasing the water resistance and lowering the contact angle. PWR increases the material's inherent porosity, which exacerbates this impact.[118]

The overall water resistance of the cellulosic papers is increased after the coating with TPR. Indeed, the paper's surface is coated with a homogeneous, cohesive layer of TPR upon application, which cross-links during the thermocompression curing process. As a result of this cross-linking, a strongly linked network is created that effectively blocks the access of water and greatly increases the hydrophobicity of the paper.[109–111]

Specifically, the TPR coating's chemical structure contributes to its efficacy, as it smoothly interacts with the cellulose and lignin. Through this integration, the surface's porosity is decreased while simultaneously being strengthened structurally, as supported by FT-IR and SEM analysis. The decreased porosity is important since it restricts the water molecules' ability to penetrate the paper, which greatly increases the water-repellent material's lifespan.[60] In contrast to the fast absorption usually observed in uncoated sheets, this prolonged water resistance is visible in the persistent high contact angle recorded after 60 seconds.

In this regard, lignocellulosic papers with a combination of PWR and TPR along with the thermocompression process is a reliable way to increase their water resistance. This method is promising for crucial applications in moist environments since it not only meets the short-term hydrophobic needs but also guarantees long-term durability and stability.

4.3.5 Tensile analysis. To enhance the mechanical properties of cellulosic papers for applications requiring greater durability and strength, researchers have explored innovative material integrations.[119,120] Among these, coating with Terpene phenolic resin (TPR) and incorporating phosphate waste rock (PWR) have demonstrated a synergistic effect on the structural integrity of the paper. These modifications are particularly crucial for adapting conventional paper materials to more demanding applications where enhanced mechanical performance is required.[119,120] In order to shed light on how PWR and TPR along with the thermocompression process improve the lignocellulosic material's performance under stress, this analysis investigates their impacts on the Young's modulus, tensile strength, and strain at breaks of produced lignocellulosic sheets (see Fig. 11).

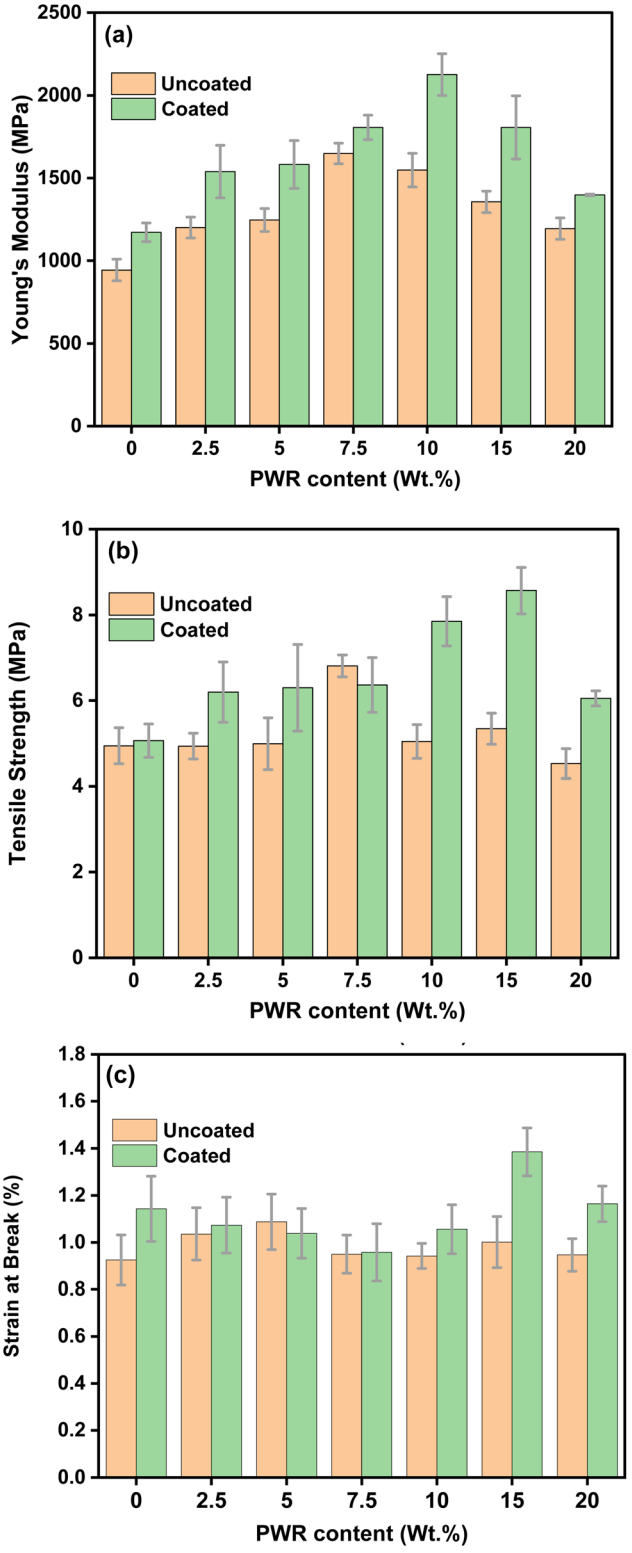

Fig. 11 Mechanical properties of the uncoated and coated papers with different PWR loadings.

The Young's modulus, a measure of material stiffness, experiences a 74.51% increase with the addition of PWR up to a concentration of 7.5 wt% compared to Uc0, with the difference being statistically significant (Student's *t*-test with Welch's correction, $p < 0.001$). The main factor responsible for this increase in stiffness is residual lignin, which acts as a natural binder in the paper matrix.[18] By enhancing the load transfer between the lignocellulose fibers and PWR particles, lignin efficiently raises the modulus and promotes a more even distribution of stress throughout the material. Furthermore, the use of pressure and heat during the thermocompression process enhances the lignin-PWR interaction even further.[18,53] The heat selectively softens the lignin, making it more able to encapsulate the PWR particles and form a solid bind with the cellulose fibers.[75] This results in a structure that is more integrated and denser, able to withstand deformation when subjected to mechanical loads. Additionally, the addition of PWR adds mineral elements that may react chemically with cellulose and lignin during thermocompression to increase the stiffness of the composite to a maximum level.[60,90] The Young's modulus, however, tends to drop above 7.5 wt% PWR. This is probably because of particle agglomeration, which causes an uneven distribution of stress and the development of structural weak areas, hence decreasing the stiffness of the material.[113]

Similarly, adding PWR up to 7.5 wt% boosts the paper's tensile strength by 37.78% relative to Uc0 ($p = 0.0163$). The increase in stress distribution and material strength is a result of thermocompression induced chemical and physical interactions between PWR particles, lignin, and cellulose fibers. The preservation of structural integrity under tensile loads is further enhanced by the heat-induced bonding between lignocellulose and the mineral constituents of PWR.[18] Tensile strength, however, noticeably decreases as PWR concentration rises above 7.5 wt%. Higher PWR concentrations cause the cellulose fiber network to become less continuous, reducing the effective load-bearing area and introducing defects that make mechanical failure easier.[113]

However, the addition of PWR up to 5 wt% results in a 17.51% improvement in the strain at break, a measure of the material's ductility. PWR particles increase the toughness of the material at these lower concentrations by stiffening the paper while also allowing for a little amount of plastic deformation.[121] The lubricating action of softened lignin during thermocompression, which enables the fibers and fillers to move relative to one another under stress and accommodates larger deformation before failure, supports this increased ductility.[113] Nevertheless, due to increased rigidity and brittleness, there is a decrease in strain at break beyond 5 wt% PWR. Elevated levels of inflexible PWR particles intensify the material's rigidity, limiting its capacity to deform elastically and ultimately causing an early breakdown when subjected to tensile strain.[113]

In particular, when combined with PWR, coating lignocellulosic sheets with TPR greatly improves their mechanical qualities.[122] Compared to Uc0, a significant improvement is shown in key measures when TPR and PWR are combined. The rigid, cross-linked network created by TPR, which effectively interacts with PWR particles and cellulose fibers, results in a maximum increase of 125% in Young's modulus at 10 wt% PWR relative to UC0 ($p = 0.0019$). Because TPR's chemical bonding creates a resilient matrix that supports larger tensile loads and mitigates possible weak areas,[121,122] tensile strength increases by 73.34% at 15 wt% PWR ($p = 0.0026$). Increased ductility and flexibility are also shown by the strain at break, which improves by 49.76% at the same concentration. This is probably because TPR, even with increasing filler content, has a microplasticizing action that lessens brittleness.[121,122] Overall, with the help of thermocompression and the combined actions of lignocellulose, TPR, and PWR, the paper is transformed into a composite material with a balanced profile of stiffness, strength, and flexibility. Maintaining this equilibrium is essential for customizing the characteristics of cellulosic papers for applications where conventional papers might not perform as intended, including outdoor settings or items subjected to varying levels of physical strain over time.

To further evaluate the performance of the proposed materials, a comparative analysis between the developed system and conventional additives and coatings reported in the literature is presented in Table 3. The selection of reference fillers was made deliberately, as purified phosphate sludge (P-PS) represents a mining by-product similar to phosphate waste rock (PWR), while limestone was chosen because it is one of the most widely used mineral fillers in the papermaking industry and shares similar major components, mainly calcium-based compounds, with PWR.[123] Regarding fillers, PWR exhibits a particle size (11.55 μm) and density (2.86 g cm^{-3}) comparable to those of conventional mineral fillers such as limestone, while maintaining a higher mechanical reinforcement effect (+37.78%). Notably, PWR was used directly without further chemical treatment, whereas P-PS required prior purification to remove heavy metals before application.[124] Despite this additional

Table 3 Comparative analysis of PWR and TPR with conventional fillers and coating materials

	Additives			Coating		
	PWR (this study)	P-PS[124]	Limestone[123]	TPR (this study)	MCO[126]	PVA/CNF[127]
Source	Mining byproduct	Mining byproduct	Natural minerals	Bio-based	Plant oils	Petroleumbased
Average particle size (μm)	11.55	10.97	0.8 to 2	—	—	—
Density (g cm^{-3})	2.86	2.73	2.7–2.9	1.02	—	—
Whiteness index ASTM (%)	60.61 ± 1.96	Light beige	87.78–90.2 (ref. 125)	—	—	—
Weight loss at 900 °C (wt%)	54.7	1	46 (ref. 134)	100	100	100
Tensile strength (%)	+37.78	−4.16	−21.0 (ref. 135)	+73.34	−28.07	+12.14
Contact angle (°)	—	—	—	122	95.5	94

processing step, P-PS still showed a decrease in tensile strength (−4.16%), similar to limestone (−21.0%), highlighting the effectiveness of untreated PWR as a functional filler at optimized loading.

In addition, according to American Standard (ASTM), PWR exhibits a whiteness index of (60.61 ± 1.96%), comparable to that of commercial fillers such as limestone,[125] further supporting its suitability for papermaking applications. In terms of coating materials, terpene phenolic resin (TPR) shows superior performance compared to bio-based and modified oil coatings. TPR achieves the highest improvement in tensile strength (+73.34%) along with enhanced hydrophobicity (contact angle of 122°), outperforming maleic anhydride-grafted camelina oil (MCO)[126] and polyvinyl alcohol/cellulose nanofiber (PVA/CNF) coating.[127] While all coatings exhibit significant thermal degradation at high temperatures due to their organic nature,[127–129] TPR provides a better balance between mechanical reinforcement and barrier properties. Overall, this comparison demonstrates that the combined use of PWR and TPR offers competitive or improved performance relative to conventional materials, while also providing a sustainable and simplified approach through the direct use of industrial by-products and bio-based resources.

Although the present study does not include extended or accelerated aging tests, previous work on mineral-filled and polymer-coated paper systems indicates that long-term exposure to environmental conditions can significantly affect performance. In mineral-filled papers, moisture-induced swelling and capillary penetration weaken fiber–filler interactions and progressively reduce mechanical strength. For instance, accelerated aging experiments on paper sheets from pine pulp revealed that increased relative humidity causes 40–68% reductions in strength properties due to hydrolysis-driven degradation, whereas the same aging conditions without water lead to only 5–22% strength loss, highlighting the critical role of moisture in durability.[130] In that study, lignin content in neutral-pH paper did not significantly influence the level of strength decline, underscoring that environmental parameters such as temperature, relative humidity, and pH must be jointly considered to objectively assess paper durability.[130,131] In the present phosphate waste rock (PWR)-filled, terpene phenolic resin (TPR)-coated lignocellulosic system, it may be particularly sensitive to moisture diffusion and thermal stresses over extended periods. Such effects can influence interfacial adhesion, coating integrity, and overall barrier performance. Previous studies on α-pinene-based terpene phenolic resins have shown that aging stability is strongly governed by the resin's softening point, with lower softening temperatures leading to reduced resistance to thermal aging and structural degradation.[132,133] These considerations highlight the importance of evaluating the long-term stability of the proposed system under realistic environmental conditions.

4.3.6 Techno-economic considerations and scalability of PWR–TPR–lignocellulosic paper. In recent years, the demand for phosphate ores has increased significantly due to their essential role in agricultural fertilizers and various industrial applications, with global production reaching approximately 223 million metric tons (Mt) in 2020.[136] Morocco is the second-largest producer, with an annual output of around 37 Mt, following China (90 Mt), and possesses nearly 70% of the world's sedimentary phosphate reserves distributed across its four main basins (Oulad Abdoun Basin, Gantour Basin, Meskala Basin, and Oued Eddahab Basin).[136,137] During open-pit mining operations, large quantities of phosphate waste rock (PWR) are generated from non-exploitable intercalations (*e.g.*, flint, limestone, and marl) and overburden layers (topsoil, clays, and marls). Recent estimates indicate that Moroccan phosphate mining sites generate between 780 and 3120 Mt of PWR annually, the majority of which is stockpiled on-site, representing both an environmental burden and an underutilized resource.[138] From a techno-economic perspective, the direct use of PWR as a filler in paper production offers a significant advantage, as it eliminates the need for costly purification or processing steps typically required for conventional mineral fillers. This not only reduces material and energy costs but also contributes to waste valorization and circular economy strategies. In parallel, the terpene phenolic resin (TPR) used as a coating material is a commercially available, produced from α-pinene.[139] Its industrial relevance is supported by a steadily growing global market, projected to reach approximately USD 2.0 billion by 2033, corresponding to a compound annual growth rate (CAGR) of about 6.2% over the period 2026–2033.[140] This growth reflects increasing demand for sustainable and environmentally friendly materials in applications such as coatings, adhesives, and rubber compounding. Overall, the combination of abundantly available PWR and commercially accessible bio-based TPR supports the scalability and potential industrial implementation of the proposed process.

5. Conclusion

This study confirmed that the combined use of phosphate waste rock (PWR) and terpene phenolic resin (TPR), together with thermocompression, strengthens the structural integrity, thermal stability, and barrier properties of carbohydrate-based papers derived from alkali- and mechanically treated date palm fibers. The residual lignin in the fibers played a key role in facilitating chemical interactions with both PWR and TPR, helping to reinforce the lignocellulosic network.

Alkali and mechanical treatments effectively modified the fiber structure, partially removing lignin and promoting defibrillation, reducing the average fiber diameter from 165.75 ± 0.86 μm to 8.49 ± 2.01 μm. Thermocompression at 130 °C, above lignin's glass transition temperature, enabled lignin redistribution within the matrix, producing a denser structure with stronger fiber-to-fiber bonding. This densification reduced water permeability and improved hydrophobicity, as reflected by a contact angle of 118° (Uc0).

The incorporation of 7.5% PWR introduced carbonate minerals (dolomite and calcite), which contributed carbonyl functionalities that interacted with the hydroxyl-rich polysaccharide matrix. These interactions increased thermal stability (T_{onset} = 306 °C, T_{max} = 335 °C), and enhanced

mechanical strength (74% gain in Young's modulus; 37% in tensile strength).

Application of TPR coating further improved these properties. The aromatic structure of TPR promoted π–π interactions with lignin and provided additional hydroxyl groups that strengthened hydrogen bonding with cellulose. This resulted in superior hydrophobicity (contact angle = 121° for C7.5) and statistically significant gains in rigidity and tensile strength, along with an increase in ductility (125%, 74%, and 50%, respectively) at 10% PWR and TPR coating.

In summary, the results validate the hypothesis that the combined incorporation of PWR and TPR, together with thermocompression, enhances the structural integrity and functional performance of lignin-containing, polysaccharide-based papers. While the present findings demonstrate clear improvements in mechanical and barrier properties, several aspects warrant further investigation. The reported performance was evaluated under controlled laboratory conditions, and long-term aging behavior, cyclic humidity resistance, and extended durability testing were beyond the scope of this study. Furthermore, the thermocompression and spray-coating processes were conducted at laboratory scale, and additional optimization will be necessary to adapt these methods to continuous industrial manufacturing. Future research should therefore focus on comprehensive durability validation, moisture cycling performance, scale-up feasibility, and quantitative assessment of repulpability to further substantiate the industrial and environmental applicability of the proposed materials.

Conflicts of interest

The authors declare that they have no known competing financial interests. The manuscript has not been published elsewhere and that it has not been submitted simultaneously for publication elsewhere.

Data availability

The data that support the findings of this study are available from the corresponding author, Fatima-Zahra SEMLALI, upon reasonable request.

Acknowledgements

This study is supported by the Moroccan Ministry of Higher Education, Scientific Research, and Innovation, along with funding provided by the OCP Foundation through the APRD research program.

References

1 A. A. de Souza Machado, W. Kloas, C. Zarfl, S. Hempel and M. C. Rillig, *Global Change Biol.*, 2018, **24**, 1405–1416.
2 S.-Y. Cheng and M.-D. Shieh, in *DRS Biennial Conference Series*, ed. D. Lockton, S. Lenzi, P. Hekkert, A. Oak, J. Sádaba and P. Lloyd, Design Research Society, Bilbao, 2022.
3 M. A. Hasan, N. Tasnim, M. T. Islam, J. Debi, R. Ahsan and P. Barua, *Notitia -časopis za Ekon. Posl. i društvene teme*, 2022, **8**, 35–51.
4 J. R. Jambeck, R. Geyer, C. Wilcox, T. R. Siegler, M. Perryman, A. Andrady, R. Narayan and K. L. Law, *Plastic Waste Inputs from Land into the Ocean*, American Association for the Advancement of Science, 2015, vol. 347.
5 W. Tan, D. Cui and B. Xi, *Front. Environ. Sci. Eng.*, 2021, **15**, 1–4.
6 P. Rath, M. Jindal and T. Jindal, *Clean. Eng. Technol.*, 2021, **5**, 100318.
7 A. Siddiqa, Z. Yhobu, D. H. Nagaraju, M. Padaki, S. Budagumpi, V. R. Pasupuleti and J. W. Lim, *Energy and Fuels*, 2023, **37**, 2498–2519.
8 R. Priyadarshi, T. Ghosh, S. D. Purohit, V. Prasannavenkadesan and J. W. Rhim, *J. Clean. Prod.*, 2024, **469**, 143151.
9 S. A. Hussain, M. P. Yadav, B. K. Sharma, P. X. Qi and T. Z. Jin, *Polymer*, 2024, **16**, 3171.
10 Z. Xiang, J. Zhang, Q. Liu, Y. Chen, J. Li and F. Lu, *Nanomaterials*, 2019, **9**, 58.
11 H. Abou-Yousef, M. El-Sakhawy and S. Kamel, *Ind. Crops Prod.*, 2005, **21**, 337–341.
12 E. S. Abd El-Sayed, M. El-Sakhawy and M. A. M. El-Sakhawy, *Nord. Pulp Pap. Res. J.*, 2020, **35**, 215–230.
13 S. Chatterjee, S. Sharma, R. K. Prasad, S. Datta, D. Dubey, M. K. Meghvansi, M. G. Vairale and V. Veer, *South Asian J. Exp. Biol.*, 2016, **5**, 271–282.
14 K. C. C. De Carvalho, S. R. Montoro, M. O. H. Cioffi and H. J. C. Voorwald, *Des. Appl. Nanostructured Polym. Blends Nanocomposite Syst.*, 2016, pp. 261–285.
15 J. Rao, Z. Lv, G. Chen and F. Peng, *Prog. Polym. Sci.*, 2023, **140**, 101675.
16 C. Vasile, M. Baican, R. Academy and P. Poni, *Polymer*, 2023, **15**, 3177.
17 M. Mariana, T. Alfatah, H. P. S. Abdul Khalil, E. B. Yahya, N. G. Olaiya, A. Nuryawan, E. M. Mistar, C. K. Abdullah, S. N. Abdulmadjid and H. Ismail, *J. Mater. Res. Technol.*, 2021, **15**, 2287–2316.
18 F. Z. Semlali Aouragh Hassani, M. H. Salim, Z. Kassab, H. Sehaqui, E. H. Ablouh, R. Bouhfid, A. E. K. Qaiss and M. El Achaby, *RSC Adv.*, 2022, **12**, 8536–8546.
19 H. Wang, J. Wang, S. Si, Q. Wang, X. Li and S. Wang, *Ind. Crops Prod.*, 2021, **170**, 113756.
20 F. Serra-Parareda, R. Aguado, Q. Tarrés, P. Mutjé and M. Delgado-Aguilar, *J. Clean. Prod.*, 2021, **313**, 127914.
21 J. Sundholm, in *Mechanical Pulping (Papermaking Science and Technology)*, ed. J. Sundholm and F. Oy, Helsinki, 1998, pp. 17–33.
22 D. Mcdonald, D. Mcdonald, K. Miles and R. Amiri, Pulp Pap. Canada-Ontario, 2004.
23 T. Pintiaux, D. Viet, V. Vandenbossche, L. Rigal and A. Rouilly, *BioResources*, 2015, **10**, 1915–1963.
24 J. Cavailles, G. Vaca-Medina, J. Wu-Tiu-Yen, J. Peydecastaing and P. Y. Pontalier, *Mater*, 2024, **17**, 1713.
25 C. I. La Fuente Arias, C. González-Martínez and A. Chiralt, *Sustain. Food Technol.*, 2023, **1**, 296–305.

26 T. Joelsson, G. Pettersson, S. Norgren, A. Svedberg, H. Höglund and P. Engstrand, *Tappi J.*, 2020, **19**, 487–499.
27 Y. Zhao, J. Yue, L. Tao, Y. Liu, S. Q. Shi, L. Cai and S. Xiao, *Int. J. Biol. Macromol.*, 2020, **158**, 1135–1140.
28 S. S. Singh, A. Zaitoon, S. Sharma, A. Manickavasagan and L. T. Lim, *Int. J. Biol. Macromol.*, 2022, **223**, 1243–1256.
29 M. Kiaei, B. Kord and R. Vaysi, *Maderas:Cienc. Tecnol.*, 2014, **16**, 495–503.
30 J. S. Han, S. Y. Jung, D. S. Kang and Y. B. Seo, *ACS Sustain. Chem. Eng.*, 2020, **8**, 8994–9001.
31 Z. Yan, Q. Liu, Y. Deng and A. Ragauskas, *J. Appl. Polym. Sci.*, 2005, **97**, 44–50.
32 N. K. Chauhan, V. S. and Bhardwaj, *Appita*, 2013, **66**, 220–228.
33 A. Tijero, M. C. Monte, A. Blanco and J. Tijero, *Tappi J.*, 2012, **11**, 43–51.
34 A. F. Lourenço, J. A. F. Gamelas, C. Zscherneck and P. J. Ferreira, *Ind. Eng. Chem. Res.*, 2013, **52**, 5095–5099.
35 N. Mechi, R. Khiari, M. Ammar, E. Elaloui and M. N. Belgacem, *Powder Technol.*, 2017, **312**, 287–293.
36 K. Bula, G. Kubicki, A. Kubiak, T. Jesionowski and L. Klapiszewski, *Polymer*, 2020, **12**, 1156.
37 Ł. Klapiszewski, A. Jamrozik, B. Strzemiecka, I. Koltsov, B. Borek, D. Matykiewicz, A. Voelkel and T. Jesionowski, *Molecules*, 2017, **22**, 1920.
38 Atalayar, Morocco, a leader in phosphate reserves and an emerging sustainable technology powerhouse, https://www.atalayar.com/en/articulo/economy-and-business/morocco-leader-in-phosphate-reserves-and-an-emerging-sustainable-technology-powerhouse/20240810170000203931.html, accessed 15 August 2024.
39 Hespress, Morocco dominates global Phosphate reserves with 70% share, finds report, https://en.hespress.com/85951-morocco-dominates-global-phosphate-reserves-with-70-share-finds-report.html, accessed 15 August 2024.
40 H. Idrissi, Y. Taha, A. Elghali, Y. El Khessaimi, A. Aboulayt, J. Amalik, R. Hakkou and M. Benzaazoua, *Mater. Chem. Phys.*, 2021, **260**, 124119.
41 J. Ai and U. Tschirner, *Bioresour. Technol.*, 2010, **101**, 215–221.
42 P. K. Kunam, D. Ramakanth, K. Akhila and K. K. Gaikwad, *Biomass Convers. Biorefin.*, 2022, **1**, 1–16.
43 V. K. Rastogi and P. Samyn, *Coatings*, 2015, **5**, 887–930.
44 F. Jahangiri, A. K. Mohanty and M. Misra, *Green Chem.*, 2024, **26**, 4934–4974.
45 V. D. Athawale and R. V. Nimbalkar, *J. Am. Oil Chem. Soc.*, 2011, **88**, 159–185.
46 N. Kimmo and R. Ville, *Finnish Pat.*, FI126885B (granted), 2011.
47 E. Y. Rhayam and A. Elharfi, *Moroccan J. Chem.*, 2016, **4**, 268–278.
48 B. S. Yew, M. Muhamad, S. B. Mohamed and F. H. Wee, *Sains Malays.*, 2019, **48**, 653–659.
49 S. Mouhoubi, M. E. H. Bourahli, H. Osmani and S. Abdeslam, *J. Nat. Fibers*, 2017, **14**, 239–249.
50 K. L. Spence, R. A. Venditti, O. J. Rojas, Y. Habibi and J. J. Pawlak, *Cellulose*, 2011, **18**, 1097–1111.
51 Z. Tanja, P. Evelyn and G. Thomas, *Adv. Eng. Mater.*, 2004, **6**, 9.
52 A. Álvarez, S. Cachero, C. González-Sánchez, J. Montejo-Bernardo, C. Pizarro and J. L. Bueno, *Carbohydr. Polym.*, 2018, **189**, 250–256.
53 B. Jiang, C. Chen, Z. Liang, S. He, Y. Kuang, J. Song, R. Mi, G. Chen, M. Jiao and L. Hu, *Adv. Funct. Mater.*, 2020, **30**, 1906307.
54 K. liyama, T. Bach-Tuyet Lam and B. A. Stone, *Plant Physiol.*, 1994, **104**(2), 315–320.
55 Ł. Klapiszewski, T. J. Szalaty and T. Jesionowski, in *Lignin - Trends and Applications*, InTech, 2018, p. 70376.
56 W. Ahmed, M. Sagir, M. S. Tahir and S. Ullah, *Phenol Formaldehyde Resin for Hydrophilic Cellulose Paper*, Springer International Publishing, 2019.
57 L. Segal, J. J. Creely, A. E. Martin and C. M. Conrad, *Text. Res. J.*, 1959, **29**, 786–794.
58 M. El Achaby, Z. Kassab, A. Aboulkas, C. Gaillard and A. Barakat, *Int. J. Biol. Macromol.*, 2018, **106**, 681–691.
59 E. Westphal and H. Seitz, *Mater. Sci. Addit. Manuf.*, 2025, **4**, 025090010.
60 F. Z. Semlali, A. Ait Benhamou, K. El Bourakadi, A. E. K. Qaiss, R. Bouhfid, J. Jacquemin and M. El Achaby, *Chem. Eng. J.*, 2023, **473**, 145268.
61 M. Y. Khalid, A. Al Rashid, Z. U. Arif, W. Ahmed, H. Arshad and A. A. Zaidi, *Results Eng.*, 2021, **11**, 100263.
62 J. Q. Lang, Q. Liu and M. G. Ma, *Carbohydr. Polym.*, 2025, **360**, 123611.
63 M. Aravindh, S. Sathish, R. Ranga Raj, A. Karthick, V. Mohanavel, P. P. Patil, M. Muhibbullah and S. M. Osman, *Adv. Mater. Sci. Eng.*, 2022, **2022**, 2009691.
64 A. El Machi, S. Mabroum, Y. Taha, A. Tagnit-Hamou, M. Benzaazoua and R. Hakkou, *Mater. Today Proc.*, 2020, **37**, 3840–3846.
65 M. J. Safi, M. Bhagwanth Rao, K. Surya Prakash Rao and P. K. Govil, *X-Ray Spectrom.*, 2006, **35**, 154–158.
66 M. Koriko, D. Zounon, S. Tchegueni, D. D. Bafai, K. A. Degbe, K. Fiaty, P. Drogui, G. Tchangbedji and J. Miner, *Mater. Charact. Eng.*, 2021, **9**, 390–405.
67 D. Walter, G. Buxbaum and W. Laqua, *J. Therm. Anal. Calorim.*, 2001, **63**, 733–748.
68 M. Amrani, Y. Taha, A. Kchikach, M. Benzaazoua and R. Hakkou, *Minerals*, 2019, **9**, 237.
69 R. Hakkou, M. Benzaazoua and B. Bussière, *Mine Water Environ.*, 2009, **28**, 206–218.
70 W. Borja, H. El Boudour El Idrissi, M. Mouiya, S. Sbi, Y. Daafi, Y. Tamraoui and J. Alami, *Ceram. Int.*, 2022, **48**, 30031–30040.
71 B. W. Chieng, S. H. Lee, N. A. Ibrahim, Y. Y. Then and Y. Y. Loo, *Polymer*, 2017, **9**, 355.
72 X. Fang, J. Xu, H. Guo and Y. Liu, *Fibers Polym.*, 2023, **24**, 505–514.
73 H. Boumediri, A. Bezazi, G. G. Del Pino, A. Haddad, F. Scarpa and A. Dufresne, *Carbohydr. Polym.*, 2019, **222**, 114997.
74 A. D. French, *Cellulose*, 2014, **21**, 885–896.

75 S. Song, S. Yuan, M. Zhang, L. Li, B. Yang, J. Nie and Z. Lu, *BioResources*, 2018, **13**, 6631–6641.
76 M. A. Hubbe and R. A. Gill, *BioResources*, 2016, **11**, 2886–2963.
77 D. Klemm, B. Philipp, T. Heinze, U. Heinze and W. Wagenknect, *Comprehensive Cellulose Chemistry*, Wiley-VCH, 1998, vol. 2.
78 M. Fazeli, S. Mukherjee, H. Baniasadi, R. Abidnejad, M. Mujtaba, J. Lipponen, J. Seppälä, O. J. Rojas and O. J. Rojas, *Green Chem.*, 2023, **26**, 593–630.
79 A. Ait Benhamou, A. Boussetta, Z. Kassab, M. Nadifiyine, M. H. Salim, N. Grimi, M. El Achaby and A. Moubarik, *Int. J. Adhes. Adhes.*, 2021, **110**, 102940.
80 A. Ait Benhamou, Z. Kassab, A. Boussetta, M. H. Salim, E. H. Ablouh, M. Nadifiyine, A. E. K. Qaiss, A. Moubarik and M. El Achaby, *Int. J. Biol. Macromol.*, 2022, **203**, 302–311.
81 I. Maria, D. Rosa, J. Maria, D. Puglia, C. Santulli and F. Sarasini, *Compos. Sci. Technol.*, 2010, **70**, 116–122.
82 H. Khalili, A. Bahloul, E. Ablouh, H. Sehaqui, Z. Kassab, F. Semlali Aouragh Hassani and M. El Achaby, *Int. J. Biol. Macromol.*, 2023, **226**, 345–356.
83 M. Jonoobi, J. Harun, A. Shakeri, M. Misra and K. Oksmand, *BioResources*, 2009, **4**, 626–639.
84 F. Z. Semlali Aouragh Hassani, W. Ouarhim, M. Raji, M. E. M. Mekhzoum, M. O. Bensalah, H. Essabir, D. Rodrigue, R. Bouhfid and A. el kacem Qaiss, *J. Polym. Environ.*, 2019, **27**, 2974–2987.
85 L. Y. Mwaikambo and M. P. Ansell, *J. Appl. Polym. Sci.*, 2002, **84**, 2222–2234.
86 A. Oushabi, S. Sair, F. Oudrhiri Hassani, Y. Abboud, O. Tanane and A. El Bouari, *South African J. Chem. Eng.*, 2017, **23**, 116–123.
87 K. E. Borchani, C. Carrot and M. Jaziri, *Cellulose*, 2015, **22**, 1577–1589.
88 C. Gao, G. Y. Xiong, H. L. Luo, K. J. Ren, Y. Huang and Y. Z. Wan, *Cellulose*, 2010, **17**, 365–373.
89 S. Cukrowicz, B. Grabowska, K. Kaczmarska, A. Bobrowski, M. Sitarz and B. Tyliszczak, *Arch. Foundry Eng.*, 2020, **20**, 119–125.
90 K. Plermjai, K. Boonyarattanakalin, W. Mekprasart, W. Phoohinkong, S. Pavasupree and W. Pecharapa, *Chiang Mai J. Sci.*, 2019, **46**, 618–625.
91 L. Hajji, A. Boukir, J. Assouik, S. Pessanha, J. L. Figueirinhas and M. L. Carvalho, *Microchem. J.*, 2016, **124**, 646–656.
92 Y. Hu, Y. Zhu, X. Zhou, C. Ruan, H. Pan and J. M. Catchmark, *J. Mater. Chem. B*, 2016, **4**, 1235–1246.
93 K. A. Trick and T. E. Saliba, *Carbon*, 1995, **33**, 1509–1515.
94 X. Zhang, N. Li, S. Han, Z. Wei and B. Dai, *Fuel*, 2022, **320**, 123844.
95 Y. Gu, M. Hummel, K. Muthukumarappan, Z. Zhao and Z. Gu, *Sci. Rep.*, 2019, **9**, 1–11.
96 J. C. Domínguez, M. Oliet, M. V Alonso, E. Rojo and F. Rodríguez, *Ind. Crops Prod.*, 2013, **42**, 308–314.
97 S. N. Ain Syed Hashim, B. Az-Zahraa Norizan, K. W. Baharin, S. Zakaria, C. H. Chia, A. Potthast, S. Schiehser, M. Bacher, T. Rosenau and S. N. Syed Jaafar, *Cellul. Chem. Technol.*, 2020, **54**, 643–652.
98 W. Gao, *Iran. Polym. J.*, 2012, **21**, 283–288.
99 M. Thébault, A. Kandelbauer, E. Zikulnig-Rusch, R. Putz, S. Jury and I. Eicher, *Eur. Polym. J.*, 2018, **104**, 90–98.
100 S. N. A. Syed Hashim, S. Zakaria, C. H. Chia, Z. Zainuddin, T. Rosenau and S. N. Syed Jaafar, *Membranes*, 2022, **12**, 106.
101 G. He and B. Riedl, *Wood Sci. Technol.*, 2004, **38**, 69–81.
102 A. Oushabi, S. Sair, F. Oudrhiri Hassani, Y. Abboud, O. Tanane and A. El Bouari, *South African J. Chem. Eng.*, 2017, **23**, 116–123.
103 A. Alawar, A. M. Hamed and K. Al-Kaabi, *Composites, Part B*, 2009, **40**, 601–606.
104 T. Alsaeed, B. F. Yousif and H. Ku, *Mater. Des.*, 2013, **43**, 177–184.
105 A. Bezazi, H. Boumediri, G. Garcia del Pino, B. Bezzazi, F. Scarpa, P. N. B. Reis and A. Dufresne, *J. Nat. Fibers*, 2022, **19**, 3770–3787.
106 S. Maou, A. Meghezzi, Y. Grohens, Y. Meftah, A. Kervoelen and A. Magueresse, *Ind. Crops Prod.*, 2021, **171**, 113974.
107 A. Ferrer, E. Quintana, I. Filpponen, I. Solala, T. Vidal, A. Rodríguez, J. Laine and O. J. Rojas, *Cellulose*, 2012, **19**, 2179–2193.
108 E. Rojo, M. S. Peresin, W. W. Sampson, I. C. Hoeger, J. Vartiainen, J. Laine and O. J. Rojas, *Green Chem.*, 2015, **17**, 1853–1866.
109 A. S. Hussein, K. I. Ibrahim and K. M. Abdulla, *Nat. Resour.*, 2011, **02**, 98–101.
110 Y. Qing, R. Sabo, Z. Cai and Y. Wu, *Cellulose*, 2013, **20**, 303–313.
111 W. Pang, R. Shi, J. Wang, Q. Ping, X. Sheng, N. Li and J. Zhang, *Mater*, 2021, **14**, 4909.
112 M. El Achaby, Z. Kassab, A. Barakat and A. Aboulkas, *Ind. Crops Prod.*, 2018, **112**, 499–510.
113 Y. Guo, L. Hu, P. Jia, B. Zhang and Y. Zhou, *Korean J. Chem. Eng.*, 2018, **35**, 298–302.
114 Y. Xin and H. Uyama, *J. Polym. Res.*, 2012, **19**, 15.
115 P. G. de Gennes, *Rev. Mod. Phys.*, 1985, **57**, 827.
116 B. J. Rhim, J. Lee and S. Hong, *Packag. Technol. Sci.*, 2007, 393–402.
117 M. N. Mirvakili, S. G. Hatzikiriakos and P. Englezos, *ACS Appl. Mater. Interfaces*, 2013, **5**, 9057–9066.
118 C. H. Xue, S. T. Jia, J. Zhang and L. Q. Tian, *Thin Solid Films*, 2009, **517**, 4593–4598.
119 M. Zhao, L. Robertsén, L. Wågberg and T. Pettersson, *Nord. Pulp Pap. Res. J.*, 2022, **37**, 624–635.
120 A. Strand, A. Khakalo, J. Kouko, A. Oksanen, A. Ketola, K. Salminen, O. Rojas, E. Retulainen and A. Sundberg, *Nord. Pulp Pap. Res. J.*, 2017, **32**, 324–335.
121 L. Alves, A. Ramos, E. Ferraz, P. Sanguino, J. Santarén, M. G. Rasteiro and J. A. F. Gamelas, *Appl. Clay Sci.*, 2023, **233**, 106823.
122 V. Chiaradia, E. Pensa, T. O. Machado and A. P. Dove, *ACS Sustain. Chem. Eng.*, 2024, **12**, 6904–6912.
123 M. A. Hubbe and R. A. Gill, *BioResources*, 2016, **11**, 2886–2963.

124 O. Bendalahcen, S. Ez-Zahraoui, R. Bouhfid, J. Alami, M. El Achaby and F. Z. Semlali, *Int. J. Biol. Macromol.*, 2025, **333**, 148853.
125 A. M. Qaid, N. Alqubati and A. M. Al-Hawbani, *Tech. Biochem.*, 2021, **2**, 28–38.
126 M. Arshad, S. Shankar, A. K. Mohanty, J. Todd, R. Riddle, R. Van Acker, G. W. Taylor and M. Misra, *ACS Omega*, 2024, **9**, 19786–19795.
127 S. Huang, X. Wang, Y. Zhang, Y. Meng, F. Hua and X. Xia, *Sci. Rep.*, 2023, **13**, 12292.
128 T. Muppaneni, H. K. Reddy, P. D. Patil, P. Dailey, C. Aday and S. Deng, *Appl. Energy*, 2012, **94**, 84–88.
129 Y.-L. Chang, S. U. Sharma, J.-P. Shiu and J.-T. Lee, *J. Electrochem. Soc.*, 2021, **168**, 100533.
130 E. Małachowska, M. Dubowik, P. Boruszewski and P. Przybysz, *Herit. Sci.*, 2021, **91**(9), 132.
131 B. Havlínová, S. Katuščák, M. Petrovičová, A. Maková and V. Brezová, *J. Cult. Herit.*, 2009, **10**, 222–231.
132 *Manfred SPIES*, 2024.
133 M. L. Binet, S. Commereuc and V. Verney, *Eur. Polym. J.*, 2000, **36**, 2133–2142.
134 A. T. Fathy, M. A. Moneim, E. A. Ahmed, A. M. El-Ayaat and F. M. Dardir, *Sci. Rep.*, 2025, **151**, 1680.
135 F. Naijian, H. Rudi, H. Resalati and H. J. Torshizi, *Appl. Clay Sci.*, 2019, **182**, 105258.
136 H. Beniddar, A. El Machi, F. E. El Abbassi, Y. Taha, M. Benzaazoua and R. Hakkou, *Constr. Build. Mater.*, 2024, **438**, 136949.
137 A. el M. Safhi, H. Amar, Y. El Berdai, M. El Ghorfi, Y. Taha, R. Hakkou, M. Al-Dahhan and M. Benzaazoua, *J. Clean. Prod.*, 2022, **374**, 134034.
138 S. Sbi, A. Aboulayt, W. Borja, S. Mansouri, H. El Boudour El Idrissi, Y. Samih, N. Semlal, H. Hannache, Y. Tamraoui and J. Alami, *Constr. Build. Mater.*, 2022, **346**, 128472.
139 *Introduction of Terpene Phenolic Resin*, Suzhou Megawide Chemicals Co., Ltd, https://www.megawidechem.com/introduction-of-terpene-phenolic-resin.html, accessed 5 January 2025.
140 Global Terpene Phenolic Resin Market Insights By Use Type, By Application, By Region and Regional Insights and Forecast2026, https://www.micromarketinsights.com/product/terpene-phenolic-resin-market/, accessed 14 April 2026.